TÉCNICO LISBOA

Magnetic sensors on flexible substrates

Ana Catarina Rosa Janeiro

Thesis to obtain the Master of Science Degree in

Materials Engineering

Supervisor(s): Prof. Diana Cristina Pinto Leitão

Examination Committee

Chairperson: Prof. José Paulo Sequeira Farinha
Supervisor: Prof. Diana Cristina Pinto Leitão
Member of the Committee: Drª Rita Joana dos Santos Macedo

November 2019

Dedico este trabalho aos meus Avós. Aos que ainda estão fisicamente, e aos que estão no meu pensamento. Estão para sempre todos no meu coração.

Agradecimentos

Quero começar por agradecer à Prof.ª Susana Freitas por me ter dado a oportunidade de conhecer o INESC há dois anos atrás, o que me permitiu ter começado a minha jornada por cá, sem dúvida que foi uma aprendizagem gigante que tive para além do que alguma vez poderia ter tido no meu curso.

Dizer um grande Obrigada à minha Prof.ª e depois orientadora deste projeto, Diana Leitão. Por me ter incentivado a arriscar e ir seguir para a frente com uma tarefa que sabíamos que não iria ser fácil, mas que me ensinou tanto. Obrigada por toda a orientação e ajuda neste processo. Deixo também um agradecimento à entidade financiadora do projeto STARCHIP em que este trabalho se inseriu.

Quero deixar também o meu agradecimento aos engenheiros de processo do INESC, que estiveram sempre dispostos a ajudar em tudo. À Rita Macedo, Ana Silva e João Mouro, obrigada por toda a ajuda e paciência na fabricação e a pensar em pontos cruciais do meu trabalho. Obrigada Verónica, por me teres aberto a porta a uma oportunidade com a qual eu não contava mas que se revelou uma surpresa muito agradável e pela qual anseio muito!

Não me podia esquecer de agradecer à Natércia por todo o carinho e ajuda que me deu, poucas pessoas têm o poder de transmitir tanto conforto :)

A todos os meus colegas e amigos que fiz no INESC. Vocês sabem quem são. Obrigada pelo companheirismo do dia-a-dia e pelos bons momentos de relax que tivemos e tanto fazem falta! O café do bistrô é realmente o melhor ;)

Às melhores pessoas que ficaram destes 5 anos. Foram a minha segunda família aqui e tornaram tudo mais fácil, ao ponto de sentir saudades de ir para as aulas e estudar no 07 mesmo quando sempre dissemos que estávamos fartos e nunca mais íamos querer voltar. Seguimos caminhos diferentes mas eles continuam sempre a cruzar-se!

Um especial obrigada à Inês, a minha amiga de sempre que eu considero família, ”adultecemos” juntas, morámos juntas e aturámo-nos muito uma à outra (mais tu a mim, I know). Obrigada por seres quem és e me teres ajudado a perceber quem sou.

Ao Tomás M., ao qual todos e quaisquer obrigados não seriam suficientes. Mas obrigada pelo apoio incondicional, por me ensinares tanta coisa que eu não sabia, por estares sempre disposto a ajudar-me, pela companhia, por me fazeres sempre acreditar que eu sou capaz do que quiser. Por tudo na realidade. Contigo foi muito mais fácil.

A toda a minha família, porque apesar da vida me levar para longe tenho sempre um lugar para onde quero voltar. À minha maninha mais nova, que é a minha companheira de vida desde sempre e alinha em tudo o que eu lhe peço, mesmo quando não gosta.

Por fim, agradecer aos meus pais, se isso for remotamente possível. Obrigada por nos colocarem sempre à frente de tudo, sem excepção. Por tudo o que me transmitiram desde pequena e fizeram para que eu hoje esteja onde estou, mesmo sabendo que isso seja longe de vocês. Obrigada por me ensinarem a dar sempre o melhor de mim.

Resumo

Sensores magnetoresistivos têm atraído muito interesse nas últimas décadas devido à sua elevada sensibilidade, baixo custo e consumo de energia e capacidade de miniaturização. Para alcançar a mesma funcionalidade em substratos flexíveis que em rígidos, as propriedades magneto-elásticas de filmes finos e a deformabilidade de polímeros devem ser profundamente estudadas.

Neste trabalho estuda-se a otimização do processo de micro-fabricação de sensores magnetoresistivos anisotrópicos em substratos flexíveis. Foram utilizados dois polímeros diferentes: Poliamida (25 e 125 µm) e Polietileno naftalato, e duas ligas ferromagnéticas foram depositadas como filme fino. Os materiais depositados são estudados em relação às suas propriedades cristalinas e magnéticas, usando técnicas de difração de raios-X e magnetómetro de amostra vibrante.

O design das estruturas foi otimizado durante a fabricação à medida que obstáculos aparecem, e microscopia eletrónica de varrimento (SEM) é usada para identificar defeitos nas estruturas fabricadas. Cinco amostras foram fabricadas com sucesso e as suas propriedades de magneto-transporte foram medidas através de uma montagem experimental personalizada para aplicar deformação, integrada no aparelho existente no INESC-MN.

O sinal máximo de AMR medido foi 0,90%, o que é muito próximo aos obtidos em silício. A PI-125 µm parece ser o melhor substrato para acomodar o sensor, pois obteve-se o melhor sinal AMR. Tem a desvantagem de não alcançar as mesmas curvaturas tão facilmente quanto PEN-75 µm e PI-25 µm. A poliamida mais fina mostra o menor sinal AMR, mas por outro lado apresenta os menores valores de campo de saturação e tensão axial, ainda com a vantagem de se adaptar a praticamente qualquer forma.

Palavras-chave: Anisotropia, Magnetoresistência, Substrato flexível, Magnetoestrição, Tensão axial induzida

Abstract

Magnetoresistive sensors have attracted much interest in the past decades due to their high sensitivity, low cost and power consumption and small size. In order to achieve the same functionality on flexible substrates as on rigid, the magnetoelastic properties of thin films and deformability of polymers must be understood in depth.

In this work we study the optimization of the microfabrication process of anisotropic magnetoresistive sensors on flexible substrates. Two different polymers were used, namely Polyimide (25 and 125 µm) and Polyethylene naphtalate and also two ferromagnetic alloys were deposited as thin films. The as-deposited materials are studied for their crystalline and magnetic properties, using X-ray diffraction and Vibrating Sample Magnetometer techniques.

The structures design has been optimized throughout the fabrication, as obstacles appear, and SEM imaging is used to identify defects in the fabricated structures. Five samples were successfully fabricated and their magneto-transport properties were measured through a custom bending setup integrated on the existing apparatus at INESC-MN.

A maximum AMR ratio of 0.90% was accomplished, which is very close to silicon counterparts. PI-125 µm seems to be the best substrate for the sensor layer, as it yielded better AMR signal, it has the drawback of not reaching the same curvature as easily as PEN-75 µm and PI-25 µm. The thinner polyimide shows the lowest AMR ratio, but on the other hand it also presents the lowest saturation field and stress values, with the advantage of conforming to almost any shape.

Keywords: Anisotropy, Magnetoresistance, Flexible substrate, Magnetostriction, Induced stress

Contents

List of Tables

List of Figures

Nomenclature

AMR Anisotropic magnetoresistance

CoFe Cobalt-iron [alloy]

H Magnetic field

H_c Coercive field

H_{dem} Demagnetizing field

H_k Anisotropy field

H_{sat} Saturation field

K_u Uniaxial anisotropy constant

λ_s Coefficient of saturation magnetostriction

M Magnetization

M_{sat} Saturation magnetization

MR Magnetoresistance

NiFe Nickel-iron [alloy]

PEN Poly(ethylene naphthalate)

PET Poly(ethylene terephthalate)

PI Polyimide

PR Photoresist

SEM Scanning electron microscope

VSM Vibrating sample magnetometer

XRD X-ray diffraction

Chapter 1

Introduction

1.1 Motivation

Magnetoresistive sensors have attracted much interest in the past decades due to their high sensitivity, low cost and power consumption and small size [1, 2]. While silicon has been the most used substrate for device fabrication, due to its useful properties as a semiconductor material, the novel applications of portable and wearable electronics have been driving a push towards materials with higher mechanical flexibility and compactness [3]. For instance, monitoring the temperature of the human body is an example of an important parameter in physiology that needs attention in terms of finding novel sensors that can be integrated with soft, flexible and curvilinear matter [4]. To this end, several research groups have been focusing on reaching the same levels of performance and sensitivity on flexible substrates as the existing on rigid counterparts.

Anisotropic magnetoresistance was the first magnetoresistive effect to be observed and implemented at industrial scale, although it was rapidly substituted by Giant magnetoresistance due to its higher MR ratio. However, this technology presents drawbacks relatively to AMR, since there is a need for external magnetic bias, increasing the volume and power consumption of the final product. Furthermore, the GMR response is not practical at low magnetic fields, yielding a small resistance change. On the contrary, AMR sensors are self-biased and can alleviate this disadvantage presenting higher sensitivities at smaller fields [5].

1.2 Framework and objectives

The main focus of INESC-MN is to produce magnetoresistive sensors on rigid substrates such as silicon and glass. However, in the past years the technological interest in flexible devices has grown, leading the development of solutions that allow adding mechanical functionality onto magnetic devices. This systems have to be adapted to existing fabrication and characterization facilities. Previous works have focused on the implementation of spin valve MR sensors on PET substrates. This thesis concentrates in testing different substrates and understanding their role in changing the intrinsic magnetic behavior of

simple thin film layers.

The goal of this dissertation is to apply the well established techniques and materials in microfabrication of rigid substrates and adapt them for use in flexible substrates, optimizing existing framework in this area. The main contribution of this work will be the microfabrication of reliable single thin film magnetoresistive structures in a meander shape, for posterior magnetic characterization under bending conditions.

To that end, several intermediate objectives have been defined:

- Characterization of Ta/$Ni_{80}Fe_{20}$/Ta and Ta/$Co_{90}Fe_{10}$/Ta thin film materials on the chosen flexible substrates: resistivity measurements, x-ray diffraction and vibrating sample magnetometer are the relevant techniques (Chapter 2);

- Optimization of fabrication processes for the patterning of meander shape structures on flexible substrate: adaptation of standard microfabrication techniques to the fabrication on flexible substrates and further implementation of optimized parameters and processes in the clean-room (Chapter 3);

- Developing of a setup for integration on the available magneto-transport characterization apparatus at INESC-MN: elaboration of bending supports and electrical connections between samples and acquisition system (Chapter 4);

- Characterization of the magneto-transport properties of the finished architectures under bending conditions: measurement of AMR curves in flat state and on bending supports and further discussion about the influence of the tested substrates on the results (Chapter 4).

1.3 State of the art

1.3.1 Principle and applications of AMR sensors

AMR sensors started to gain popularity around the 1980's as high density read heads for tape and disk drives [2], but these were rapidly substituted by GMR technology, as the latter yields higher MR ratios. Other common applications include automotive wheel speed and crankshaft sensing, compass navigation, vehicle detection, current sensing, and many others [6].

Practically all AMR devices assume a "barber pole" structure composed of aluminum stripes sputtered on permalloy (Py) strips that deflect the direction of the current by 45^{o} with respect to the direction of magnetization, so that the change in resistance is linear and the largest. Four of these elements are connected in a Wheatstone bridge (Fig. 1.1), in which the sensitivity of two branches have the opposite direction than the other two, in order to double the signal output.

They are often composed of a single layer of Permalloy ($Ni_{80}Fe_{20}$) thin film designed in a meander shape to induce a strong anisotropy and maximize the length of the sensing element.

The sensitivity of the bridge is often expressed as mV/V/Oe, which means that if the middle term (bridge voltage) is set to 5 volts, and its sensitivity is 3 mV/V/Oe, then the output gain will be 15 mV/Oe. Output levels of 1 µV can be achieved, resulting in a magnetic resolution of 67 µOe [7].

Although the bridge configuration is the most common, there are other types of AMR sensors, which was the case in the work of Ger et al., that fabricated a rolled-up structure with a layer of Permalloy in silicon substrate for cell sensing. The cells were labeled with magnetic nanoparticles, which in turn were attracted towards the sensors and MR measurements were performed. The tests were made with 2D (planar) and 3D (rolled-up) structures. The results in the 2D sensor showed that the switching field and MR ratio changed from 2.08 mT to 2.31 mT and 0.194% to 0.193% respectively. On the other hand, the 3D structure was more sensitive to the nanoparticle attachment, as the switching field and MR ratios changed from 2.67 mT and 0.279% to 4.34 mT and 0.05%. Such a difference can be due to the influence of the stray field of the magnetic cell, which becomes more relevant in the 3D structure since it encloses the cell (Fig. 1.2). This 3D biosensor has the potential to integrate microfluidic channels for cell detection and counting with high accuracy which is important for health monitoring and diagnosis applications [8].

Vehicle detection is fundamental for collecting information from moving vehicles on the road, including traffic volume, occupancy rate and vehicle speeds. For this purpose, AMR sensors that sense the earth's magnetic field (EMF) have been studied by M.H. Kang et al. Four magnetoresistors are mounted into a wheatstone bridge and if the resistance in one or more devices is altered by the change in EMF caused by a moving vehicle, the sensor produces an output signal. The tests were carried out in a highway (Fig. 1.3), and the sensors were placed with the sensitivity axis perpendicular to the road's surface, since they observed that the vehicles running on other lanes interfered with the sensors. When a vehicle passes over the AMR sensor, the EMF suffers variations caused by all the different dipole moments of the vehicle parts. They observed that each vehicle type (vans, trucks, buses, etc) had a different magnetic signature that was translated in the output curve. An experiment during low-speed congested traffic situation was also conducted, the vehicles were traveling below 10 km/h, on average. The vehicles were counted by the sensor with an error of 0.3 $\%$ [9].

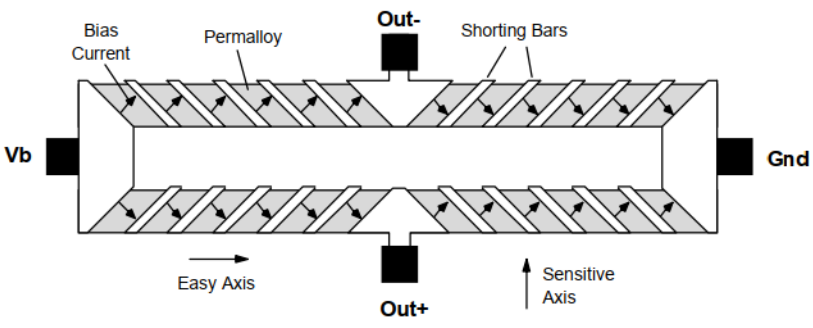

Figure 1.1: AMR sensor barber pole confirguration. (Reused from [7] © Honeywell, Inc).

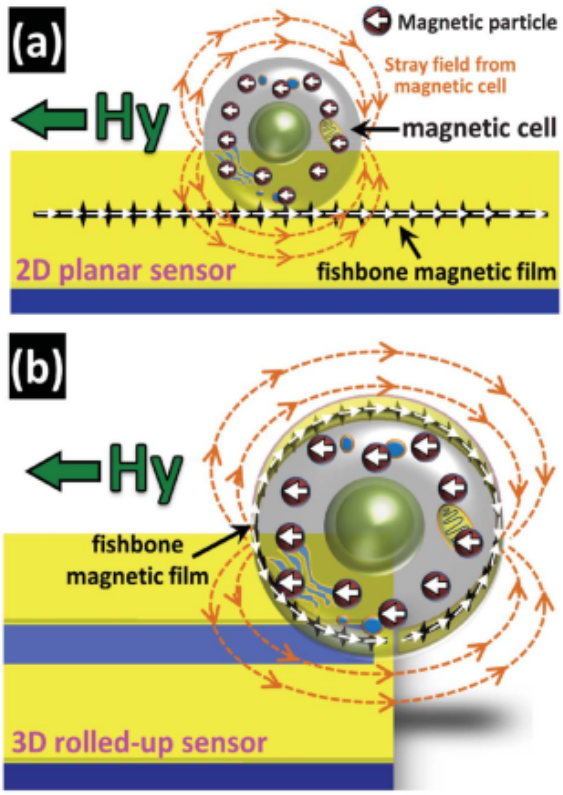

Figure 1.2: Schemes of the influence of the stray field on 2D and 3D structures. (Reused from [8] © The Royal Society of Chemistry 2013).

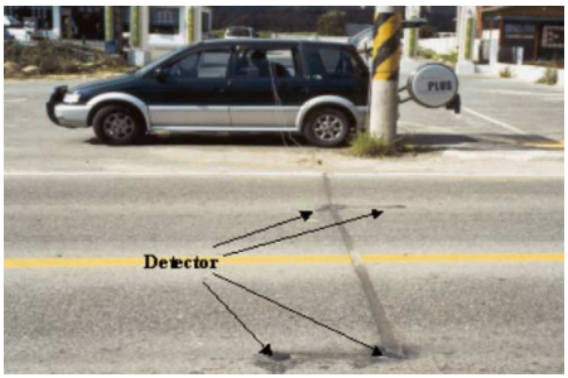

Figure 1.3: Photograph of experimental site and position of the AMR sensors. (Reused with permission from [9] © 2004 Elsevier B.V.).

1.3.2 Fabrication on flexible substrates

Flexible substrates are gaining more attention in the electronics field of study due to their applications in wearable devices, displays, rollable solar panels and health monitoring systems [5]. When it comes to device fabrication, flexible polymers can offer lower costs when compared to silicon, less fabrication steps and feature high mechanical flexibility [10].

In contrast to sensors based on silicon substrates, the effect of the flexibility of polymers in the performance of electronic systems needs special attention. Mechanical deformation related to stretching

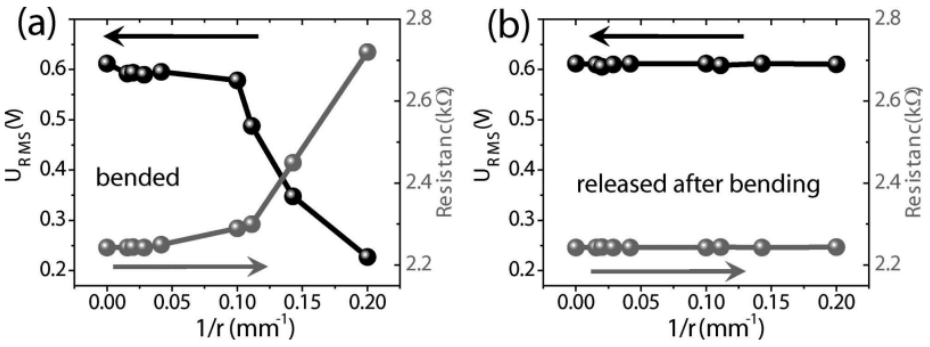

Figure 1.4: Electrical output and resistance of flexible AMR sensor mounted on surfaces with different curvature radius (from flat to r = 5 mm). (a) Voltage and resistance under bending. (b) Voltage and resistance after release. (Reused with permission from [5]

and bending may affect the reproductibility and retention of device characteristics [11], so it is of great importance to understand this effects and develop techniques to overcome this.

Wang et al. successfully fabricated self-biased AMR magnetic field sensors with a sensitivity limit around 1.5 $\times$ 10^{-3} Oe at 3 Hz and a sensitivity of 42 T^{-1}, close to the value on rigid Si substrate and superior to GMR counterparts. To attain this, 100 µm PET (polyethylene terephthalate) foils were used as substrate with 30 nm of permalloy thin film deposited by magnetron sputtering. Before deposition, a buffer layer of photoresist (PR) was added to improve surface roughness of the PET foil. This sensor was also designed in wheatstone bridge configuration, and the metal leads were accomplished by deposition of 100 nm of gold. Along with the PET/PR/Py sensor, they also fabricated a sensor without PR as buffer layer and a Py layer on Si/SiO_2 for comparison. The magnetoresistance was measured through 4 point probe method, and an increase of the AMR ratio was observed, from 0.76% on PET/Py to 0.96% on PET/PR/Py. Additionally, bending tests were performed on the sensors by mounting them onto cylinder objects with different radii. After bending the sensors 50 times, measurements showed that the resistance and output voltage of the sensors were stable with curvature radius $>$ 10 mm. For smaller radii, there was an increase in resistance and output voltage, but these values returned to the original when the sensors were released to their flat state, as can be seen in Fig.1.4. This recovery of the properties of the AMR sensors indicates that these have outstanding deformation stability, which can sustain a significantly large amount of strain even with a wrapping radius down to 5 mm [5].

GMR sensors came along after AMR, demonstrating higher magnetoresistance ratios between 10% to 80%. This effect occurs in a multilayer sandwich of two magnetic layers that are separated by a thin non-magnetic film [10]. Nowadays, research groups are focusing in the accomplishment of this technology on flexible substrates, with a particular interest in Kapton, a polyimide (PI) with desirable thermosetting properties with high thermal and chemical stabilities [11]. Based on the inverse magnetostriction effect of magnetic layers, Kwon et al. fabricated spin-valve structures of Ta/NiFe/CoFe/Cu/Ni/IrMn/Ta on PI substrate (125 µm). NiFe and Ni are the free and pinned layers, respectively, by stress application through bending of the flexible layers. Stack deposition was accomplished by DC magnetron sputtering with a magnetic field of around 20 mT to set the easy axis of the material. By application of downward

bending stress along the easy axis, magnetic anisotropy of the free layer decreases and it becomes relatively free to rotate with the applied field, and the anisotropy of the pinned layer increases. Repetitive bending stress by the mechanical bending machine accumulates these effects and, as a result, the magnetic configuration of the free and pinned layers is settled down after 200 bending cycles (Fig. 1.5).

The MR ratio of 2.3% measured in the initial flat state gradually increases to 7.0% in the after flat state for 100-times bending due to the enhanced magnetic anisotropy of the pinned layer in spite of the reduction of the anisotropy in the free layer. Posteriorly, a prototype spin-valve sensor cell array was fabricated for the detection of microbeads. At zero external field, the sensing cells had a voltage output of 35.4 mV, indicating the existence of magnetic beads on the cell window area because the stray field from the beads affects magnetization reversal of the free layer [11].

Other engineering polymer that has been gaining a lot of ground in flexible electronics is PEN (polyethylene naphthalate), which has been reported as superior to PET with higher mechanical strength, namely yield tensile stress and Young's modulus, heat resistance and dimensional stability [12, 13].

Structural health monitoring (SHM) can be complex and time consuming due to difficult access to some construction elements. For this reason, this area has been attracting researchers to improve the process of guaranteeing the safety of buildings, bridges, tunnels or even dams. SHM involves procedures that use integrated measuring systems to collect data and transform them to information on the actual state of the surveyed structures. Currently this is achieved mainly by typical measuring systems with strain gauges or fiber-optic sensors [14].

These inspections require many sensors because of the large areas and complexity of the structures, which increases its costs significantly. The overall cost of such an array can be reduced significantly if all the strain sensors are fabricated by printing methods using cost-effective materials. Zymelka et al. propose the fabrication of printed devices, featuring low cost and rapid, large-area manufacturing. This was accomplished by laminating a PEN foil (50 µm) with a copper sheet (16 µm) by hot pressing and etching of the copper layer to define metal leads and electrodes. On the top of the conductive lines, a 4 $\times$ 4 array of 16 sensors was screen printed using thermosetting graphite paste with the help of a stainless steel mesh. The diameter of each sensor was 16 mm. The sensors were cured in a conventional oven at 150 °C for 30 min, and the final electrical resistance of the unit sensor was 88.9 $\pm$ 4.6 kΩ. Lastly, connectors with flexible flat cables were soldered to the corresponding copper electrodes on the

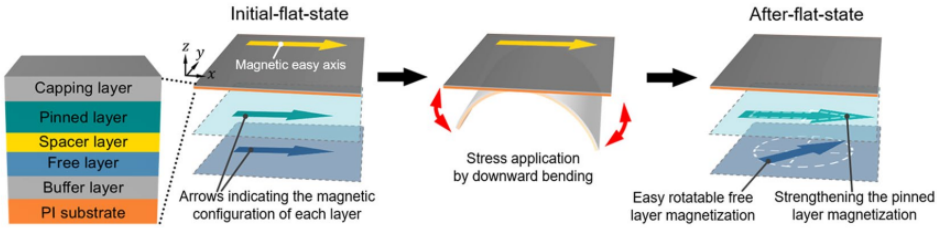

Figure 1.5: Schematic illustration of magnetic configuration of a spin-valve in PI substrate before and after downward bending stress along the magnetic easy axis. (Reused with permission from [11] © The Author(s) 2018).

substrate and the structure was covered with self-adhesive PET-based laminating sheets. Bending tests were carried out in a tensile test machine in the laboratory, with strain gauges installed on the bottom to use as reference strain measurements. Twenty bending cycles up to around 130 $\mu\varepsilon$ were applied. In some applications, such values of strain would be considered low, however, based on available literature [14], typical strain levels that are measured during normal traffic on undamaged elements of bridges are relatively low and do not exceed 80 $\mu\varepsilon$. Tests with temperature variation were performed and values of relative change in electrical resistance were converted directly to strains, although no mechanical deformation was applied, so the apparent strain is because of the changes in temperature. Results shown that slight temperature fluctuations may influence the measurements significantly, despite the fact that a full Wheatstone-bridge enables compensation for these variations.

After the laboratory tests, the sensors were installed on a highway bridge (Fig. 1.6) in three different spots (a metal girder and concrete pier), namely one of them was placed exactly over a crack on the concrete, as seen in Fig. 1.6(d) and (e). There was a significant difference between the results registered on the metal girder and the pier. Because the metal girder experienced no damage, and is in general more elastic than concrete, the sensors showed uniform changes in the output signals in which the amplitude depends on the instantaneous load on the bridge. Typical strain registered during the passage of heavy vehicles was $\pm$ 25 $\mu\varepsilon$.

In contrast, sensors installed in the concrete pier exhibit nonuniform strain results, especially the ones on top of the crack, that showed significantly higher strain levels. This reveals a novel approach and alternative to high cost current solutions with the use of flexible polymers as substrate for fabrication [15].

GMR multilayer elements (Co/Cu and Py/Cu) can be directly fabricated on 1.4 µm ultrathin PET foils. This substrate is fully compatible with lithography and lift-off processes, which is key to large-area and low-cost manufacture. The PET substrate temporarily adhered to a 125 µm thick polymer to help handling during the fabrication process. A positive lithography lift-off process was performed to define sensor stripes of 1 $\times$ 16 mm^2. The magnetoresistive layers were deposited by magnetron sputtering,

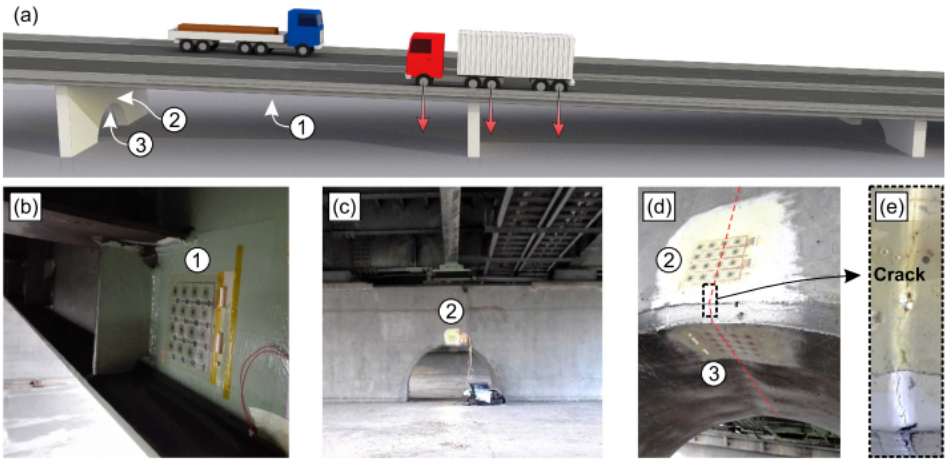

Figure 1.6: (Reused from [15])

and after lift-off, electrical contacts were realized using thin copper wires and silver paste. This sensors demonstrated remarkable potential for smark skins application, or medical implants [4].

The same authors published a work where they chose 60 µm thick PDMS (poly(dimethylsiloxane)) membranes that are mechanically pre-stretched up to 25% $\times$ 25% strain of their size. This is fundamental to achieve higher stretchability without inducing cracks in the sensor layer. With this approach, they increased from 4% to 30 % the stretchability of GMR multilayers without crack formation.

A poly(acrylic acid) (PAA) layer was spin-coated on top of a Si wafer and pre-baked at 90 ºC for 5 min before the lithographic standard process. Deposition of GMR multilayers on top of PAA was again accomplished by magnetron sputtering and electrodes were defined on a second lithography level, followed by e-beam evaporation of Cr/Cu layers. The receiver membranes of PDMS were prepared and stretched using a frame with clamps, and then both donor and receiver substrates were activated with oxygen plasma at 50 W. Subsequently they were brought into contact on a hot plate under weight and pressure of about 10 kPa for 30 min. After, the whole structure was immersed in a solvent to dissolve the sacrificial layer and release the Si, so the sensors stayed imprinted on PDMS [16].

1.4 Theoretical Background: Magnetic anisotropy and Magnetoresistance

On the atomic level, different sources that cause magnetic anisotropy can be identified. The spontaneous magnetization of the domains tends to lie along one or more easy directions determined by crystal structure, atomic-scale texture or sample shape. This tendency is represented by the anisotropy energy E_a, in which the leading term is:

$$E_a = K_u \sin^2 \theta \tag{1.1}$$

where θ is the angle between magnetization and the anisotropy axis and K_u is the anisotropy constant, with units of J m^{-3}. These values can range from less than 1 kJ m^{-3} to more than 10 MJ m^{-3}.

The anisotropy field, H_a is derived minimizing the energy term, and is defined as the field needed to saturate the magnetization of a uniaxial crystal in a hard direction:

$$H_a = \frac{2K_u}{\mu_0 M_s} \tag{1.2}$$

Since $\mu_0 M_s \sim 1$ T for a typical ferromagnet, H_a values are of the order of 2.5 mT to more than 32 mT [17].

There are essentially three causes of anisotropy in a material: shape, magnetocrystalline and induced anisotropy. These are explained below.

1.4.1 Shape anisotropy

This is not an intrinsic property of the material, as it depends on sample shape. It derives from the demagnetizing field that is generated within each domain of the ferromagnetic sample. In the case of thin films, it is more energetically favorable for magnetization to lie in the film plane and the bigger the aspect ratio of the sample, the largest is the demagnetizing field created, and thus the largest is the shape anisotropy of the sample. In eq. 1.3 is shown the shape anisotropy contribution for the total energy of the system [17]:

$$E_d = \frac{1}{2}\mu_0 M_s^2 \cos^2\theta \tag{1.3}$$

μ_0 is the free space permeability, M_s is the spontaneous magnetization and θ is the angle between magnetization and the perpendicular to the film plane. Typical values for shape anisotropy are around 200 kJ/m^3.

1.4.2 Magnetocrystalline anisotropy

The three 3d ferromagnetic elements (Fe, Ni, Co) show a different saturation behavior when magnetized in different directions. In the case of iron, the easy directions for magnetization are the cube edges $\langle 100\rangle$, and the diagonals $\langle 111\rangle$ are hard directions. For nickel it is the other way around, since it has a FCC lattice instead of BCC. On the other hand, cobalt has only the hexagonal axis [001] as easy direction. Therefore, these materials are easily magnetized if the field is applied in the same direction as the easy axis. The magnetocrystalline anistotropy energy has a leading term represented by:

$$E_a = K_1 \sin^2\theta \tag{1.4}$$

The anisotropy constant, K_1 values can range from 0.1 to 10^4 kJ/m^3.

This form of anisotropy arises from two distinct sources, namely single-ion contributions and two-ion contributions.

In single-ion anisotropy, the contribution is due to electrostatic interaction of the orbitals with the potential created by the crystal itself. The crystal-field interaction stabilizes a particular orbital and through the spin-orbit interaction, the magnetic moment aligns in a certain crystallographic direction.

On the other hand, the two-ion contribution reflects the anisotropy of the dipole-dipole interaction. In terms of energy, head-to-tail configuration is the most favorable, so that magnets tend to align in this form. If we extend this to the entire lattice, the spins will all be aligned in the same direction, creating anisotropy. For certain cases such as cubic lattices, the total sum cancels and this effect vanishes. However, in noncubic lattices (i.e. hexagonal), this dipole interaction is a considerable source of FM anisotropy.

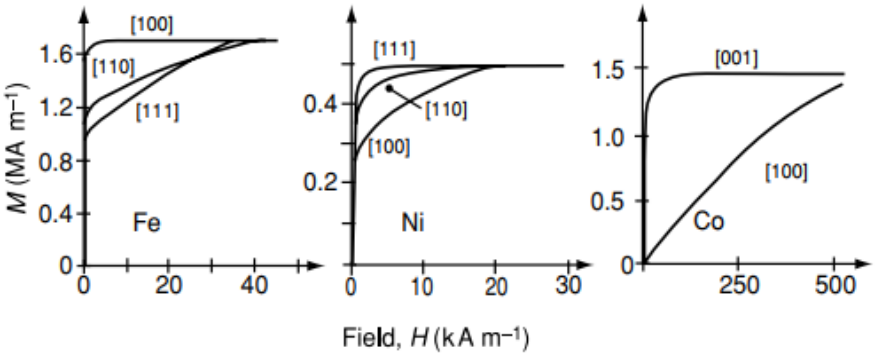

Figure 1.7: Magnetization curves of single crystals of iron, cobalt and nickel [17].

1.4.3 Induced anisotropy

There are several ways of inducing uniaxial anisotropy in a crystal. For example, annealing in a magnetic field, promoting atomic diffusion to build texture in the film, creating a preferred orientation for magnetization. Similar texture can be achieved by atomic deposition of films in a magnetic field of around 10 mT, which was one of the methods used in this work.

Applying stress, σ to some materials can also cause magnetic anisotropy. The magnitude of this phenomena is described as:

$$K_{u\sigma} = \frac{3}{2}\sigma\lambda_s \tag{1.5}$$

where λ_s is the saturation magnetostriction constant. Magnetocrystalline anisotropy also contributes to this effect, since the largest values of uniaxial anisotropy are found in hexagonal and other uniaxial crystals, whereas the smallest are found in cubic and amorphous alloys [17].

1.4.4 Magnetostriction

Magnetostriction can be generally described as the change in size of a material due to its magnetization process. This change can be either in volume, which in this case is isotropic and reflects a change in interatomic spacing, or linear in the direction of magnetization.

In general, if θ is the angle between the magnetization and the easy axis:

$$\lambda(\sigma) = \frac{\lambda_s(3\cos^2\theta - 1)}{2} \tag{1.6}$$

In cubic crystals there are two principal values for magnetostriction, for example, in iron we have λ_{100} = 15 $\times$ 10^{-6} and λ_{111} = - 21 $\times$ 10^{-6}. Considering the isotropic average:

$$\lambda_s = \frac{2}{5}\lambda_{100} + \frac{3}{5}\lambda_{111}, \tag{1.7}$$

Iron saturation magnetostriction is λ_s = - 7 $\times$ 10^{-6}.

Linear strain changes are related to the rotation of domains as the magnetization saturates. Two

distinct effects fall in this category, namely the Joule and Villari effect. James Joule observed in 1842 the change in size of a nickel rod during a magnetization process.

The Villari effect (also known as inverse magnetostriction) happens when mechanical stress is applied to a demagnetized sample, modifying its easy axes for magnetization, which will be the focus of this work. This phenomenon falls in the category of induced anisotropy and is commonly classified as magnetoelastic anisotropy. The magnetoelastic energy density term can be writen as:

$$E_{ms} = -\lambda_s \frac{\sigma}{2}(3\cos^2\theta - 1) \tag{1.8}$$

with θ being the angle between magnetization and the strain axis. This energy has a range of values that goes up to 100 kJ m^{-3} [17]

1.4.5 Magnetoresistance

Magnetoresistance (MR) is described as a change in resistance of a material in the presence of a magnetic field (eq. 1.9). The magnetoresistive device will tend to align its magnetization with the applied field resulting in a variation of resistance. The minimum and maximum resistance registered define the magnitude of the magnetoresistance effect.

$$MR(\%) = \frac{R_{max} - R_{min}}{R_{min}} \times 100 \tag{1.9}$$

MR can arise due to several mechanisms, such as anisotropic (AMR) [10], giant (GMR) [18] and tunneling magnetoresistance (TMR) [19], and thin film-based devices have been developed implementing each of these phenomena [17]. This work focuses only on AMR based technology.

1.4.6 Anisotropic Magnetoresistance

The AMR effect was discovered in 1857 by William Thompson, by observing that the resistivity of Ni varies slightly with the direction of current, relative to the direction of magnetization [20]. This mechanism occurs in 3d transition metals and is due to spin-orbit coupling, demonstrating the interaction between the spin of the conduction electrons and the crystal lattice. An increase in the resistivity of the system occurs as the majority s-electrons are scattered into (minority) d-orbital states. This anisotropic scattering has a probability of occurring that depends on the orientation of magnetization relative to the flowing current. If the d-orbitals are parallel to the current direction, the resistivity is higher, whereas if they are perpendicular, it will be lower [21]. As depicted in Fig.1.8, the change in resistivity depends on θ, the angle between the direction of the current and magnetization. Eq.1.10 describes this phenomenon, where $\rho_\perp$ and $\rho_{//}$ refer to the resistivity values at θ = 90º and θ = 0º, respectively [22].

$$\rho(\theta) = \rho_\perp + (\rho_\parallel - \rho_\perp)\cos^2\theta \tag{1.10}$$

Typical AMR values at room temperature are $\sim$ 5% for NiFe and CoFe bulk alloys [22] and lower for

Table 1.1: Summary of saturation magnetization (M_s), anisotropy constants (K_1) and magnetostriction coefficients (λ_s) of 3d ferromagnetic elements and $Ni_{80}Fe_{20}$ [17].

	M_s (kA/m)	K_1 (kJ m^{-3})	λ_s (10^{-6})
Fe	1710	48	- 7
Ni	488	- 5	- 35
Co	1440	410	- 60
$Ni_{80}Fe_{20}$	830	- 1	2

patterned thin films ($\sim$ 2%) [23]. This reduction is caused by additional scattering, for example at grain boundaries and film interfaces.

Before 1997, the main industry application for AMR sensors were in read heads for magnetic hard disk drives, which are basically storage disks, but with advances on technology, AMR heads were quickly replaced by systems based on GMR [25]. Nevertheless, thanks to their simple design, low cost, robustness and temperature stability, these sensors were introduced in a wide range of applications, such as the automotive industry, consumer electronics, biotechnology and more recently, the focus has been flexible electronics as it will be shown further in this document. In the first two, they are used for current sensing, position, speed and angle sensing and even in compasses for the detection of the earth's magnetic field. As for the biotechnology field, these are mostly applied in bimolecular detection in protein assays using magnetic tags or microfluidic systems for magnetic bead manipulation [10].

In table 1.1, the saturation magnetization, anisotropy constants, and magnetostriction coefficients are shown for the 3d ferromagnetic elements, as well as $Ni_{80}Fe_{20}$ alloy.

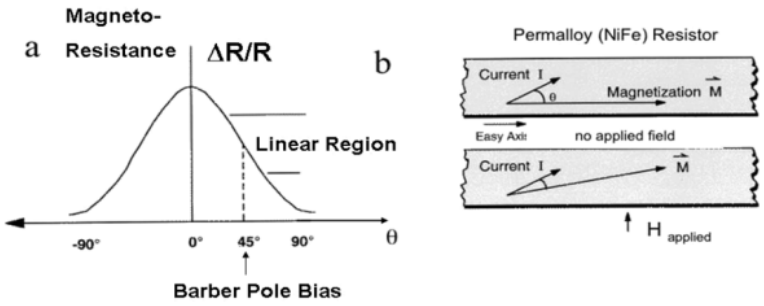

Figure 1.8: AMR sensor working principle: (a) magnetoresistance variation with angle; (b) change in the angle between magnetization and current with applied magnetic field. (Reused with permission from [24] © 2006 IEEE.

Chapter 2

Thin-film characterization: results and discussion

This chapter focuses on the techniques used to deposit thin-films on flexible substrate, as well as the further characterization work that was done in order to assess the quality of the films.

2.1 Substrate preparation

Prior to all depositions, the substrate needs to be as clean as possible, in order to promote good adhesion at the interface and proper film growth.

The first step in preparing the substrate for fabrication is to cut it in the desired shape and dimensions. In the present case, the chosen sizes were 1 $\times$ 1 inch and 1 $\times$ 2 inches.

Next, a cleaning step is performed by submerging the substrate in alconox solution and ultrasounds at room temperature for about one hour. Finally the substrate is cleaned with isopropyl alcohol (IPA) and deionized (DI) water to remove the alconox solution from its surface and stored.

The following substrates were used in this study: polyimide (PI), that goes by the commercial name of Kapton HN, with a thickness of 25 and 125 µm. This material has a high thermal and mechanical stability, two key properties when microfabricating flexible sensors and is synthesized by polymerizing an aromatic dianhydride and an aromatic diamine [29]. It has been used successfully at temperatures that range from -269 ºC to 400 ºC, so it is suitable for a diverse range of fields that go from electronics, fiber optics, insulation to automotive sensors. In Table 2.1 values of the Poisson coefficient ν, tensile

Table 2.1: Summary of mechanical, thermal and electrical properties of PEN [26, 27], PET [27, 28] and Kapton HN [29].

Substrate	ν	E_s (GPa)	α (10^{-6} K^{-1})	ρ (Ω.cm)	T_{max} (ºC)	T_g (ºC)
PEN	0,3	5-5.5	20-21	10^{15}	115	120
PET	0,37-0,44	2-4	20-80	10^{14}	115-170	78
Kapton HN (PI)	0,34	2.5	20	1.5×10^{17}	250-320	360-410

modulus E_s, coefficient of thermal expansion α, resisitivity ρ, upper working temperature T_{max} and glass transition temperature T_g, among others are summarized for the mentioned polymers.

In addition, a polyethylene naphthalate (PEN) foil with a thickness of 75 µm was also used. This material is very similar to polyethylene terephthalate (PET), but each benzene ring is replaced with a naphthalene ring, and it has been reported as superior to PET, as previously stated in the state of the art.

Although the standard micro-fabrication methods still show challenges when working with flexible substrates, the latter are gaining more attention for applications such as flexible printed circuits, organic semiconductor substrates and wearable devices [30]. There are some properties that need to be taken into account when choosing a suitable material for the desired applications.

2.2 Material selection and deposition

2.2.1 Permalloy: $Ni_{80}Fe_{20}$

One of the chosen materials for this work is the permalloy, with a stoichiometry of 80% Ni and 20% Fe of the deposition target. It is a soft magnetic alloy, widely used in the magnetic industry due to its high permeability, low coercivity and small magnetic anisotropy [31]. This particular percentage is known to have near zero magnetostriction, which makes it a good base comparison for a study with materials that have a significant magnetostricion constant [32]. These films are mostly used in AMR sensors, with a working temperature that goes up to 225 ^oC [33], but also in sensing layers of advanced magnetoresistive sensors based in GMR and TMR.

2.2.2 $Co_{90}Fe_{10}$

Cobalt-iron based thin films are mostly used because of their high saturation magnetization values. In the past years they have also been attracting attention as an alternative to NiFe alloys, due to the possibility of obtaining softer magnetic properties with a suitable underlayer. That is why one of the main challenges has been to obtain CoFe thin films with lower coercivities, as they normally range from 5 - 10 mT [34], for the purpose of magnetic recording devices. CoFe alloys have a higher anisotropy than NiFe and larger magnetostriction constant. These materials are also key components of multilayered stacks for MR sensors.

2.2.3 Deposition techniques

Two deposition techniques were employed during this work.

A Nordiko 3000 ion-beam system was used for depositing $Ni_{80}Fe_{20}$. It consists of a fully automated machine equipped with two RF ion sources corresponding to a deposition and an assist/etch gun. Inside the chamber we can find 6 targets and a substrate table, capable of rotation and pan angle adjustment.

This machine allows the deposition of both metallic and oxide films, as well as ion milling, through the assist gun.

Samples are mounted in approximately 6 inch metallic plates, that are placed horizontally in a cassette with a total of 8 slots. The cassette is placed in the load lock, which is then pumped by a turbomolecular pump, along with a mechanical pump that makes a primary vacuum as a backing to the turbo. When a base pressure of about 10^{-5} Torr is achieved, the batch process can start and a robot arm will transport the samples to the main chamber. The chamber is preferentially always pumped, with a base pressure of 10^{-8} Torr [25].

The RF antennas produce plasma from an inert gas (Xe for deposition and Ar for etching) via a series of voltage-biased grids, which is accelerated into the chamber. The deposition gun is directed to the material target, and when the beam strikes it, material is ejected towards the sample. On the other hand, the assist gun is aimed at the substrate table and hits the sample directly, removing material.

There are several working conditions that can be tuned depending on the materials we are processing, and these will be briefly discussed further in the next section.

On the other hand, $Co_{90}Fe_{10}$ was deposited in a Nordiko 2000 system, a magnetron sputtering machine featuring 2 RF and 4 DC power supplies. Maximum sample size is 2×2 square inch and thus has a smaller load lock and deposition chamber.

In DC deposition mode, the metallic target serves as cathode, while the substrate is the anode, and plasma is created between these two by argon injection into the chamber. Positive ions are accelerated by an electric field superimposed on the target, colliding and ejecting atoms from its surface, which will be deposited on the substrate. Furthermore, the cathode has a magnetron that creates a magnetic field to confine the plasma near its surface trapping electrons, thus enhancing both the efficiency of the initial ionization and allowing lower working pressures. This reduces background gas incorporation in the growing thin film and energy losses through gas collisions when comparing to normal DC or RF sputtering [35].

To deposit insulating films such as MgO or Al_2O_3, RF power is used to avoid charge build up [36].

2.3 Material characterization

2.3.1 Resistivity (4-probe method)

Electrical resistivity is an intrinsic property of bulk materials that dictates how much a material can oppose the flowing of electric current. To understand how resistivity varies from bulk materials to thin films is of great interest for the field of design and performance of circuits. The thickness of these conductors are in the order of a few dozens of nanometers, where it is more likely for charge carriers to interact with the boundaries as current flows. This quantity is therefore very dependent on film thickness, grain size and the presence of defects [37].

Assuming an uniform cross section, the resistivity is given by:

$$\rho = R\,\frac{A}{l} \tag{2.1}$$

where R is the resistance, $A = w \times t$ is the area of the cross-section and l, w, t are the length, width and thickness of the material, respectively. The SI units for this quantity are Ω.m but all resistivity values will appear in $\mu\Omega$.cm for simplification.

Firstly, the resistance of thin metallic films grown on glass and polymer (calibration samples) was measured with the four-probes method. For this purpose, a simple system built at INESC-MN with 4 probes equally spaced was connected to a Keithley 2000 multimeter with 4 wire sensing mode, and current was swiped from -5 mA to 5 mA in steps of 1 mA. Electric current is applied through the outer probes, while voltage is measured across the inner probes, diminishing contact resistance and increasing the accuracy of the measurements. With the obtained results, linear fits were used to determine the resistance of each sample, along with the associated error. In this case, the length l corresponds to the distance between the 2 inner probes, as it is the effective length being measured, l = 0.84 $\pm$ 0.001 cm. This parameter, along with resistance and cross-sectional area allowed the calculation of the resistivity; these values are displayed in Table 2.2. To determine the cross-sectional area, the nominal thickness of the films (200 Å) was used, since the deposition machines have a highly optimized deposition rate. The resistivity deviation was obtained through an error propagation formula.

The resistivity value obtained for the $Ni_{80}Fe_{20}$ film on glass is in accordance with results previously observed at INESC using the same deposition technique [21]. As for the resistivities on flexible substrates, these samples have a layer of 200 Å in comparison with the 500 Å on glass, which results in an increase in the resistivity value. Moreover, these substrates have a higher surface roughness than the conventional rigid substrates, leading to films with smaller grain sizes. This implicates more roughness at interfaces, promoting scattering and diffusion at grain boundaries, thus increasing resistivity [31].

$Co_{90}Fe_{10}$ resistivity values are in accordance with [23]. In addition, this material also exhibits an increase in resistivity when deposited on flexible substrates.

2.3.2 X-ray diffraction (XRD)

In order to better understand the influence of these flexible substrates on film growth, x-ray diffraction was used on samples both with $Ni_{80}Fe_{20}$ and $Co_{90}Fe_{10}$ with a layer of 500 Å (with bottom and top Ta). A total of 9 samples were measured, corresponding to the substrates alone and two films in the three

Table 2.2: Measured resistivity values (presented in $\mu\Omega$.cm) for samples with a thickness of 200 Å, except when stated otherwise.

Material/Substrate	Glass	PI-25	PI-125	PEN
$Ni_{80}Fe_{20}$ alloy	21.95 $\pm$ 0.08 (500 Å)	47.80 $\pm$ 0.13	42.90 $\pm$ 0.22	44.10 $\pm$ 0.28
$Co_{90}Fe_{10}$ alloy	8.24 $\pm$ 0.03	15.30 $\pm$ 0.04	16.40 $\pm$ 0.04	14.60 $\pm$ 0.04
Au	5.42 $\pm$ 0.16 (1100 Å)	-	-	-
$Al_{98.5}Si_1Cu_{0.5}$	4.73 $\pm$ 0.46 (3100 Å)	-	-	-

Table 2.3: Acquisiton conditions for x-ray diffraction of $Ni_{80}Fe_{20}$ and $Co_{90}Fe_{10}$ thin films (unless stated otherwise in the text).

Parameters	
Tube voltage (kV)	40
Tube current (mA)	20
2θ range (º)	5-50
2θ step (º)	0.02
Acqusition time per step (s)	3

substrates.

This is a non-destructive technique and allows the probing of the crystallographic structure of the sample, as well as its chemical composition and physical properties. X-ray photons hit the surface of the sample and are scattered by the atoms in the periodic lattice. Those x-rays that are in phase create constructive interference, at the incident angles given by Bragg's Law (eq.: 2.2):

$$n\lambda = 2\,d\sin\theta \tag{2.2}$$

where the integer n is the order of reflection, λ is the x-ray wavelength (in this case, a Mo K_α generator with λ = 0.70930 Å), d_{hkl} is the spacing between crystal planes (where (hkl) refers to the Miller indices of planes in a crystal) and θ is the angle formed by the incident beam and the normal to the reflecting lattice plane.

The analyses were carried out in a Siemens D5000 diffractometer, where the samples are mounted in the center of the holder to maximize the intensity of the reflected wave. The equipment is controlled by a computer software where one inserts the desired parameters, namely the 2θ range and step and acquisition time per step. These conditions are summarized in Table 2.3.

The resulting spectra will present peaks if the material turns out to be crystalline, which needs to be analyzed in order to understand what is the preferential direction of scattering, thus discovering the crystal structure.

A fitting function is applied to each peak, namely a Lorentzian profile (Eq. 2.3), which fit better to the results (χ^2/df values are lower than with a Gaussian profile) and is used to extract the values of the peak centroid ($2\theta_0$) and full width at half maximum (FWHM), that is given by w.

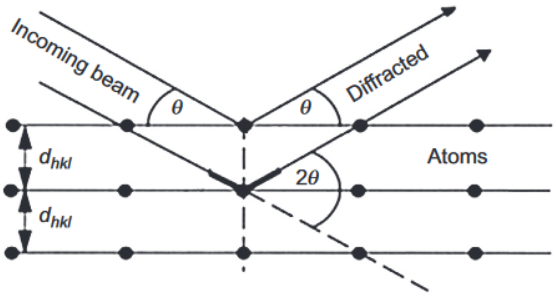

Figure 2.1: Geometrical condition for diffraction within a crystal [38].

$$y = \frac{a}{1 + \left(\frac{2\theta_0 - 2\theta}{w/2}\right)^2} + b \tag{2.3}$$

From the peak positions $2\theta_0$, the distance between adjacent atom planes d_{exp} was calculated using Bragg's law.

The main contributing factor for peak broadening in a polycrystalline sample is the size of the crystallites (grains). These are subdomains of a larger crystal exhibiting a continuous lattice of atoms and a certain orientation. The size of these crystallites can be estimated in XRD analysis through the Scherrer equation (eq. 2.4), where D is the average crystallite size, λ the x-ray wavelength, β the FWHM of the sample broadening contribution and K, a factor depending on the peak shape and crystallite geometry, among other attributes. Assuming spherical crystallites, K = 0.9 [39].

$$D = K\frac{\lambda}{\beta\ \cos\theta} \tag{2.4}$$

These results are summarized in Table 2.4, along with reference values taken from literature of interplanar distances.

Figure 2.2 depicts the spectra obtained in these measurements, where the plot in fig. 3.14b shows the curves of the three flexible substrates with no film deposited. This allows us not only to later compare with the film diffraction spectrum but also to have an idea about the crystallinity degree of the substrates.

The 2θ sweep values were chosen based on literature and consecutive tests, so all the possible peaks both from substrates and films would appear in the plots.

According to the information present on the product datasheets, the polyimide substrates are amorphous, typically showing only broad peaks, as seen in fig. 3.14b. These peaks appear in the range of 5º to 15º (2θ), which are in accordance to literature results [40].

The PEN curve shows a broad peak characteristic of the amorphous phase, but on the other hand, presents also a sharp peak at $2\theta \approx 12$º. This is probably due to its fabrication process, which causes its partial crystallization, as stated on the datasheet. Crystalline polymers as PEN present two condensed forms of polymer chains, crystalline and amorphous. The ratio of crystalline parts in the whole polymer volume is changeable by various processes, the most common being mechanical stretching techniques, such as cold drawing, as well as thermal treatments.

Although references [13] and [27] for PEN showed a larger number of peaks in XRD, those observations were made under temperature tests above T_g that crystallized the polymer. In comparison, the peak obtained at 2θ = 11.96º corresponds to the 26.3º value acquired by Odaka et al. [13]. The calculated interplanar distance is 3.40 Å, which is very close to the result obtained by these authors, 3.33 Å. This peak corresponds to the (-1 1 0) plane in the crystal form α, which is known to be orthorhombic.

In Figure 3.14c the three $Ni_{80}Fe_{20}$ curves are shown, each corresponding to the film deposited on a different substrate. For all three substrates, a peak appears at $2\theta \approx 20$º. According to literature, this is a highly crystalline peak related to the (1 1 1) orientation in face-centered cubic (FCC) structures [41]. Two weaker peaks should also appear, corresponding to orientations (2 0 0) and (2 2 0), but that was

Table 2.4: Fitting parameters, average crystallite sizes, calculated and reference interplanar distances and Miller indices for the peaks in the thin films XRD spectra. All samples have a buffer and cap layer of Ta 100 Å.

Sample	$2\theta_0$ (°)	w (°)	χ^2/df	D (Å)	d_{exp} (Å)	d_{teor} (Å)	(hkl)
PEN 75 µm	11.96	0.632	8.67	58.17	3.40	3.33 [13]	-1 1 0
$Ni_{80}Fe_{20}$ 500 Å PEN	20.21	0.275	6.12	135.17	2.02		
$Ni_{80}Fe_{20}$ 500 Å PI-25	20.15	0.431	10.62	86.26	2.03	2.04 [42]	1 1 1
$Ni_{80}Fe_{20}$ 500 Å PI-125	20.09	0.262	7.77	141.78	2.03		

not the case in this work, probably due to the high degree of texture of the deposited thin films, which exhibit a strongly preferred orientation.

The results yielded the same interplanar distance for all three samples, which is a good indicator that the film is growing in the same structure on the different substrates. In addition, the obtained value for this property is in accordance to d_{teor} [42]. The crystallite sizes are very similar when looking at the thicker substrates (PEN and PI - 125), but the 25 µm kapton sheet yields a smaller result. Guittoum et al. verified that the average crystallite size for $Ni_{80}Fe_{20}$ on kapton did not depend on film thickness and was around 140 Å, although the substrate thickness used in their experiment was not specified [31]. Since the diffraction peak of this sample is highly coincident with the others, the influencing variable is w (FWHM) which gives us information about peak broadening effects. Namely, the bigger w, the more broad the peak is. This difference could be related to the position of the sample when mounted on the holder. Flexible substrates have a high tendency to bend, so if the surface is slightly curved during measurements this could affect the peak shape and position, consequently affecting the grain size estimate.

$Co_{90}Fe_{10}$ samples did not yield meaningful results, but it is known from literature that its structure is BCC, normally exhibiting the (110) and (200) peaks.

2.3.3 Vibrating sample magnetometer (VSM)

A study of the magnetic properties of the samples was performed prior to fabrication, for validation of the sensors characterization results, and also as another test to the thin films quality. For such, a vibrating sample magnetometer (DMS 1660 system) was used to acquire a hysteresis loop for each sample.

A sample is fixed to the tip of a glass rod that vibrates between two electromagnets that generate a programmable magnetic field. When the test starts, a magnetic field H is applied and the sample becomes magnetized in its direction. Once the sample begins to vibrate, it induces changes in the magnetic flux that are collected by the sensing coils in terms of voltage, which is proportional to the magnetization of the sample. Changes in the signal are converted to magnetization M values by a software to produce a graph of M versus H.

The samples were measured in two directions, the easy axis (induced by a magnetic field during film deposition) and the hard axis, orthogonal to the first. A magnetic field from -100 mT to 100 mT

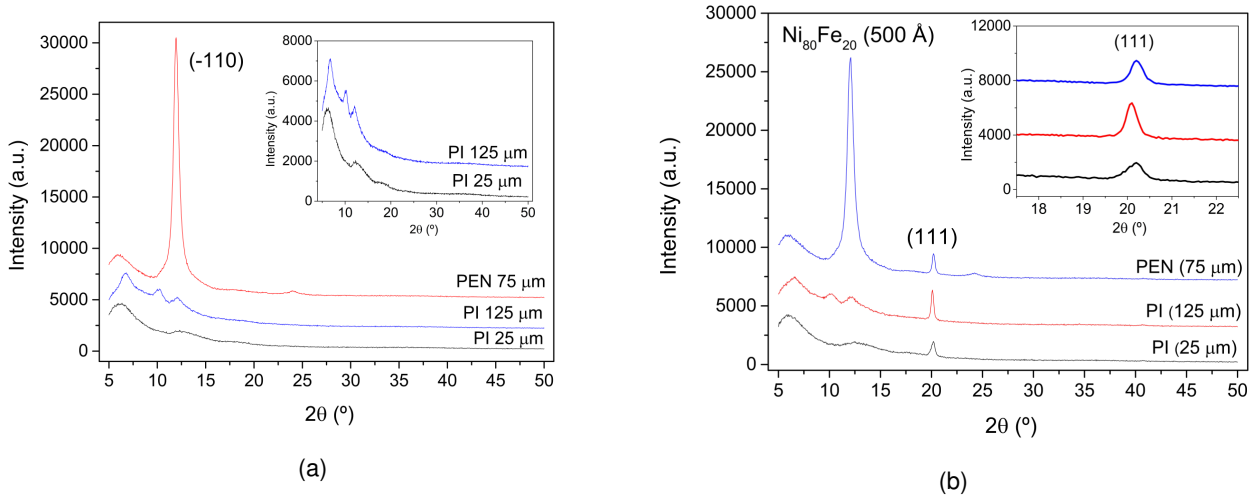

Figure 2.2: XRD spectra: a) PEN, PI 25 µm and PI 125 µm with no film on top; Inset: PI 25 µm and PI 125 µm curves shown in detail; b) Ta 100 Å /$Ni_{80}Fe_{20}$ 500 Å/ Ta 100 Å on different substrates; Inset: $Ni_{80}Fe_{20}$ (111) peak zoomed on different substrates.

was applied during all measurements and the results are shown in fig. 2.5. We can extract valuable information from both curves, namely the coercive (H_c) field from the first and anisotropy (H_k) field and saturation magnetization (M_s) from the latter. The coercive field can be described as the magnetic field necessary to revert the magnetized state of a material, whereas the anisotropy field is the field needed to saturate the magnetization of an uniaxial crystal in the hard direction. Saturation is the state reached by a material when an increase in the external applied field cannot increase the magnetization further.

For comparison, 200 Å of Ni were deposited in Alcatel by magnetron sputtering on PI 125 µm with a buffer and cap layer of Ta 100 Å. Table 2.5 presents a summary of the values extracted from the magnetization plots. The first column refers to the normalized magnetization, the second to the coercive fields (H_c) and the third depicts the anisotropy fields (H_k).

According to the Stoner-Wohlfarth model [17], when the field is applied in the direction of the easy anisotropy axis, the coercivity is equal to the anisotropy field:

$$H_c = \frac{2K_u}{\mu_0 M_s} \tag{2.5}$$

where K_u is the sum of the magnetocrystalline and shape anisotropy [17]. The experimental values do not differ significantly, but H_k is higher than H_c in all samples except Ni. This difference is probably due to the effective anisotropy constant being larger than what the model considers, due to other contribution such as the field induced anisotropy during film deposition.

$Co_{90}Fe_{10}$ results present a higher coercivity and anisotropy field than $Ni_{80}Fe_{20}$, as expected, since it has a much higher contribution from the magnetocrystalline anisotropy. Furthermore, the coercive field values are in accordance to literature [43].

$Ni_{80}Fe_{20}$ coercivity values are also as expected, it has a low coercive and anisotropy field due to its low magnetostriction [44]. Values for the anisotropy field are in accordance with [32], [45] and as for the coercive field, very similar results were obtained on Kapton HN [46].

As for the substrate influence, it appears to be almost negligible. When looking at both $Ni_{80}Fe_{20}$ and $Co_{90}Fe_{10}$ few differences can be observed, as all values are of the same order. However, there seems to be a slightly influence on $Co_{90}Fe_{10}$, as there is a bigger dispersion of the H_c and H_k values.

From H_k results, the effective anisotropy constant was estimated through the following equation:

$$K_u = \frac{H_k \mu_0 M_s}{2} \tag{2.6}$$

with $\mu_0 = 4\pi \times 10^{-7}$ J/A^2/m and theoretical M_s values of 830 kA/m [17] and 1600 kA/m [47] for $Ni_{80}Fe_{20}$ and $Co_{90}Fe_{10}$, respectively. These values represent a rough but valid estimate for the anisotropy, with $Co_{90}Fe_{10}$ values with one order of magnitude bigger than $Ni_{80}Fe_{20}$.

Table 2.5: Magnetic properties of unpatterned samples with 200 Å of sensing layer encapsulated with 100 Å Ta. M/M_{sat} (normalized magnetization), H_c (coercive field) and H_k (anisotropy field) were extracted from the plots; K_u is the effective anisotropy constant.

Sample	M/M_{sat}	H_c (mT)	H_k (mT)	K_u (J/m^3)
Ta 100 Å /Ni 200 Å/Ta 100 Å // PI-125	0.89 $\pm$ 0.03	2.5	0.9	-
Ta 100 Å/$Ni_{80}Fe_{20}$ 200 Å/ Ta 100 Å // PEN	0.89 $\pm$ 0.03	0.4	0.7	290
Ta 100 Å/$Ni_{80}Fe_{20}$ 200 Å/ Ta 100 Å // PI-25	0.87 $\pm$ 0.01	0.3	0.5	208
Ta 100 Å/$Ni_{80}Fe_{20}$ 200 Å/ Ta 100 Å // PI-125	0.91 $\pm$ 0.03	0.4	0.7	290
Ta 100 Å/$Co_{90}Fe_{10}$ 200 Å/ Ta 100 Å // PEN	0.89 $\pm$ 0.01	3.7	4.4	3520
Ta 100 Å/$Co_{90}Fe_{10}$ 200 Å/ Ta 100 Å // PI-25	0.82 $\pm$ 0.01	4.1	5.5	4400
Ta 100 Å/$Co_{90}Fe_{10}$ 200 Å/ Ta 100 Å // PI-125	0.91 $\pm$ 0.03	3.0	3.9	3120

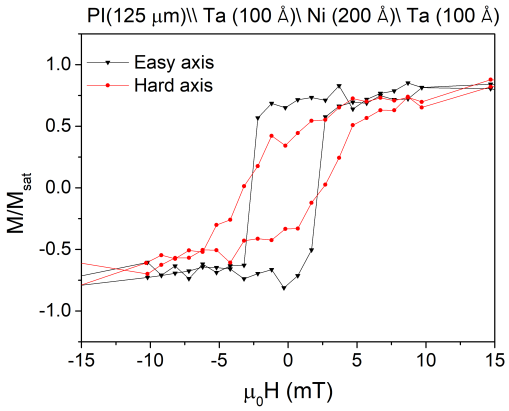

(a)

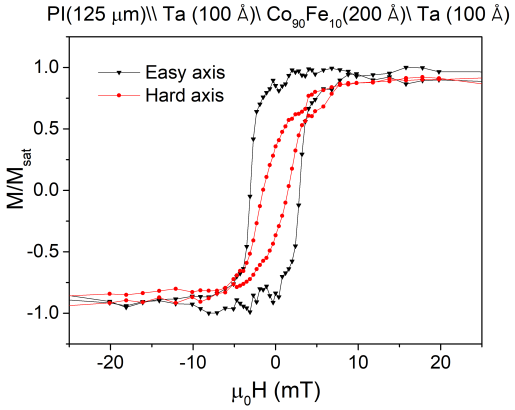

(b)

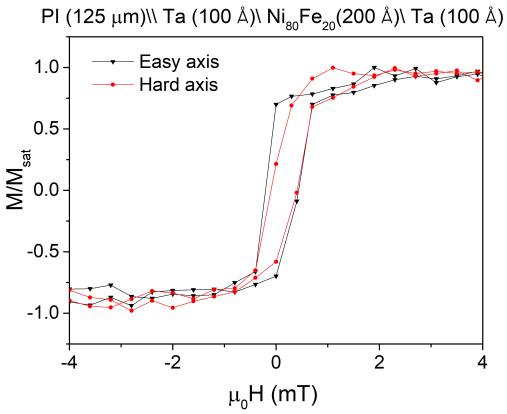

(c)

Figure 2.3: VSM plots of PI - 125 µm samples: (a) Ta/Ni/Ta, field sweep from -600 to 600 mT; (b) Ta/$Co_{90}Fe_{10}$/Ta, field sweep from -100 to 100 mT; (c) Ta/$Ni_{80}Fe_{20}$ /Ta, field sweep from -100 to 100 mT.

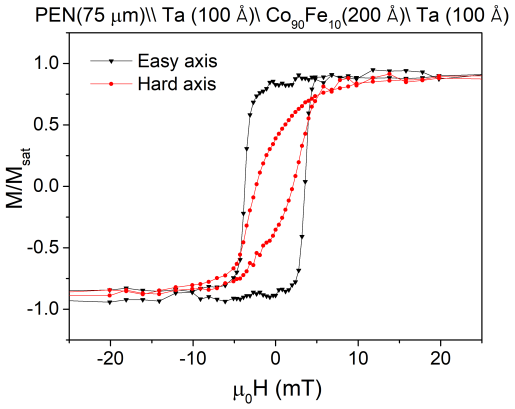

(a)

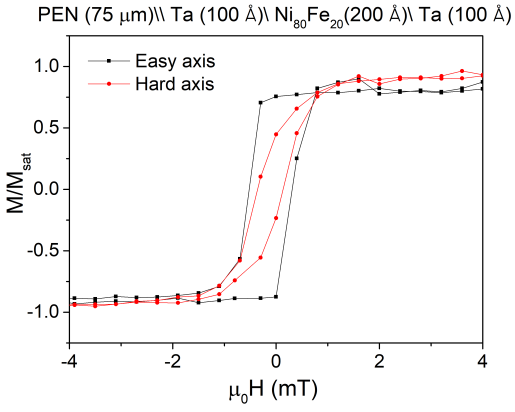

(b)

Figure 2.4: VSM plots of PEN - 75 µm samples: (a) Ta/$Co_{90}Fe_{10}$/Ta, field sweep from -100 to 100 mT; (b) Ta/$Ni_{80}Fe_{20}$ /Ta, field sweep from -100 to 100 mT.

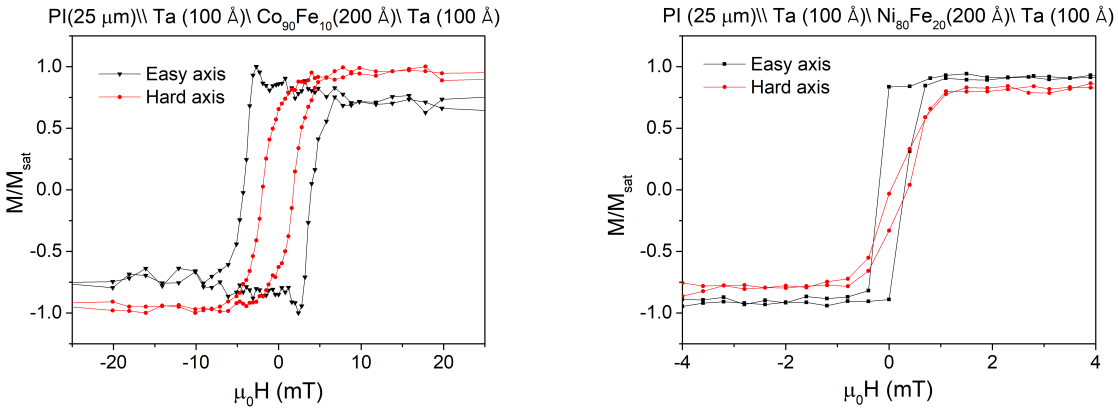

Figure 2.5: VSM plots of PI - 25 µm samples: (a) Ta/$Co_{90}Fe_{10}$/Ta, field sweep from -100 to 100 mT; (b) Ta/$Ni_{80}Fe_{20}$ /Ta, field sweep from -100 to 100 mT.

Chapter 3

Fabrication process

As details of substrate cleaning were explained earlier in the document, and can also be consulted in the runsheet attached, the next step of fabrication is to deposit the thin films. $Ni_{80}Fe_{20}$ and $Co_{90}Fe_{10}$ alloys are the sensing layers (with 200 Å), and both were encapsulated with 100 Å of Ta, serving as a bottom layer to improve adherence of the film and promote epitaxial growth and as top to protect the sensor and prevent oxidation. As stated above, two different deposition methods were used, ion beam deposition and magnetron sputtering.

A general overlook of the process is illustrated in fig. 3.1 and each step designation is explained in Table 3.1.

3.1 1st lithography: sensor layer

After material deposition, the next task is to define the sensors. This operation consists of defining the sensor shape, and is accomplished by a direct-write laser (Heidelberg DWL 2.0) that exposes a photosensitive polymer (photoresist) through the desired mask, to be revealed after development. Prior to lithography, the samples are coated with photoresist (PR), which can be positive if it becomes soluble

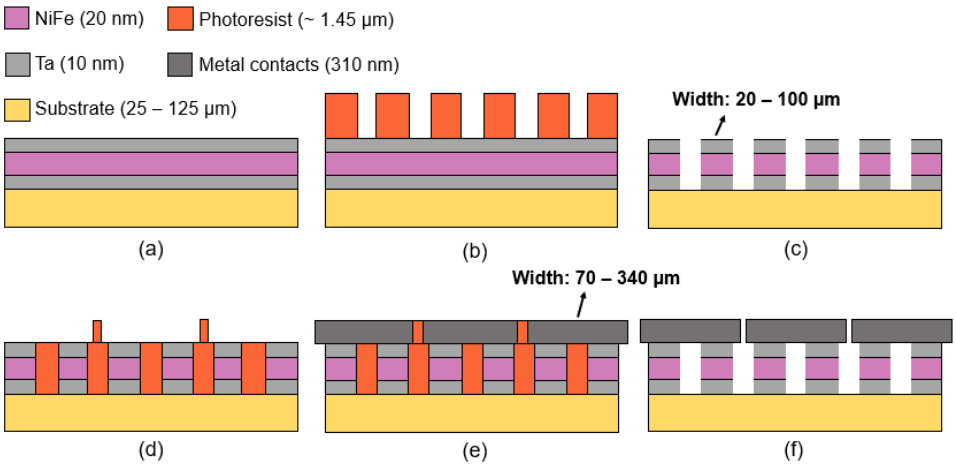

Figure 3.1: Fabrication process overview.

Table 3.1: Fabrication process summary of Fig. 3.1.

Step	Sketch	
0	(a)	Stack deposition
1	(b)	1^{st} level of lithography to design and protect the sensor (inverted mask)
2	(c)	Etching and photoresist strip
3	(d)	2^{nd} level of lithography to define the electrical contacts (non-inverted mask)
4	(e)	Deposition of electrical contacts (AlSiCu or Au)
5	(f)	Lift-off to remove the photoresist

after exposure to light (for this instance), or negative and it will harden upon exposure. This step is made in an automatic SVG track system, which has two stations: one for coating, and the other for development. A sample is mounted on a 6-inch holder wafer that goes on a spin-coater previously programmed for a speed of 2500 rpm in order to achieve a PR thickness of 1.45 µm, followed by a baking step of 60 seconds at 85 °C to build up the resist profile and evaporate any remaining solvent. To define which areas are to be exposed, a mask file is created in AutoCAD software, and subsequently converted and divided into 200 µm wide stripes, which are exposed in sequence. This equipment has a minimum feature size of 0.8 µm whereas the alignment between two levels of lithography can be made with a precision of 0.1 µm, using a control software that automatically recognizes an alignment cross and centers one layer in accordance with the other. The last step requires heating the sample again at 85 °C for 60 seconds, cool for another 30s and the exposed areas of PR are dissolved after a bath and spin with a chemical developer (TMA238WA). Depending on what is the next step of fabrication, the patterned mask may be inverted or not-inverted. An inverted mask is used to protect structures, for example for etching, whereas a not-inverted is applied when the next stage is depositing contacts for lift-off. For this work, only 2 levels of lithography were required to fabricate the sensors, the first is the sensing layer and the second defines the electrical contacts that allow the characterization of the structures. A two layer mask was created in AutoCAD and was continuously altered throughout the fabrication of several samples.

The first layer is inverted, and it is the one that underwent more changes. The substrate size was 1 $\times$ 2 inches, and the mask die was 19000 $\times$ 35000 µm. In Figure 3.2 parts of the three versions of the mask are shown so the first layer is seen in detail. The first version served as test, only one sensor was designed and the five pairs of contacts were all redundantly connected to the sensor. It had a projected nominal resistance of 1kΩ so we could have a fairly good electrical output. Each stripe is 150 $\times$ 15000 µm. The next two versions of the mask had five sensors plus several others for testing. In Table 3.2 the different sizes of the designed sensors for the second and third version of the mask is depicted, the idea was to test the practicability of the fabrication with several sensor dimensions, and to see if it was possible to obtain working sensors to characterize in the end.

The lithographies were carried out with 85$\%$ of the laser energy and the sample was placed on a proper holder with small holes that allows the sample to flatten through vacuum suction of the laser stage. After every lithography, it is crucial to observe the designed structures in an optical microscope,

Table 3.2: Different sensor sizes from versions 2 and 3 (width $\times$ length) in µm.

Sensor	Size
S1	20 $\times$ 800
S2	40 $\times$ 800
S3	80 $\times$ 1000
S4	100 $\times$ 2500

whether to search for defects or check if the photoresist is successfully developed. If it passes the optical inspection, the sample moves to the next phase.

3.2 Etching by ion-beam

The etching step was performed in Nordiko 3000, the same machine used for $Ni_{80}Fe_{20}$ deposition that was described in the previous chapter. This step is made in order to remove all the material from the sample, except the sensor stripes protected with photoresist. The etching is only supposed to stop when the substrate is reached. The working conditions such as power, voltage, current and working pressure are displayed in Table 3.3. The etching rate of the machine was calibrated for a spin valve stack, but it works for almost any material and is approximately 1 Å/s with the substrate pan at 60º. Since all samples had 400 Å of material, in the first samples fabricated, the programmed etching times were 400 seconds. This rate worked for $Ni_{80}Fe_{20}$, but it wasn't enough to remove all the material from $Co_{90}Fe_{10}$ samples. This is due to this material being harder than $Ni_{80}Fe_{20}$, so the etching time had to be prolonged for 500 or even 600 seconds in some cases. To assure that the etching step is completed, a multimeter is used in the substrate area to test for any electrical contact, since the polymers are not conductive,

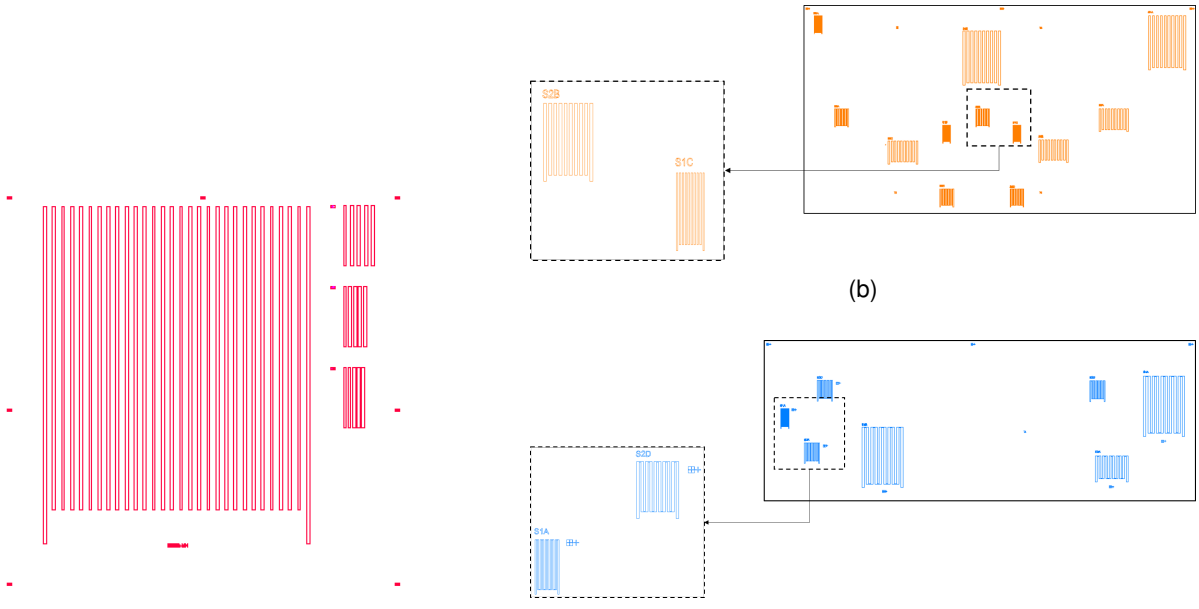

(a) (b) (c)

Figure 3.2: First layer of the different mask versions. (a) Version 1; (b) Version 2; (c) Version 3;

there should be no electrical output.

The etching steps didn't yield any visible deffects in the samples, regardless of the material or substrate. This is observable in fig. 3.4. Figure 3.4a shows a $Ni_{80}Fe_{20}$ S4 test sample from mask version 3 on PI - 125 µm. Figures 3.4b and 3.4c display S2 sensors from version 2, on PEN and PI - 25 µm respetively. All sensors are successfully defined, although in PEN and PI - 125 µm the surface looks smoother but this is due to the substrate thickness being larger that PI - 25 µm.

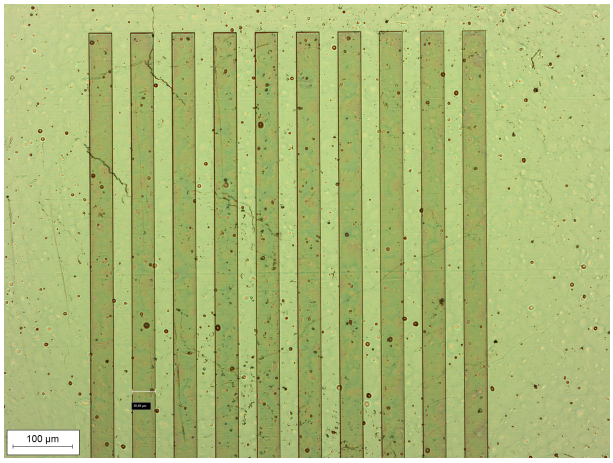

Figure 3.3: Example of $Ni_{80}Fe_{20}$ S2 sensor in PI-25 µm after the first lithography. The stripes (darker color) represent the sensor protected with photoresist. Background imperfections are features of the substrate and do not affect performance.

Table 3.3: Etching conditions in N3000 for $Ni_{80}Fe_{20}$ and $Co_{90}Fe_{10}$.

RF Power (W)	V+ (V)	I+ (mA)	V- (V)	I- (mA)	Gas flux (sccm)	W.P. (Torr)
54	487.5	28.1	193.3	1.8	7.9	1.7×10^{-4}

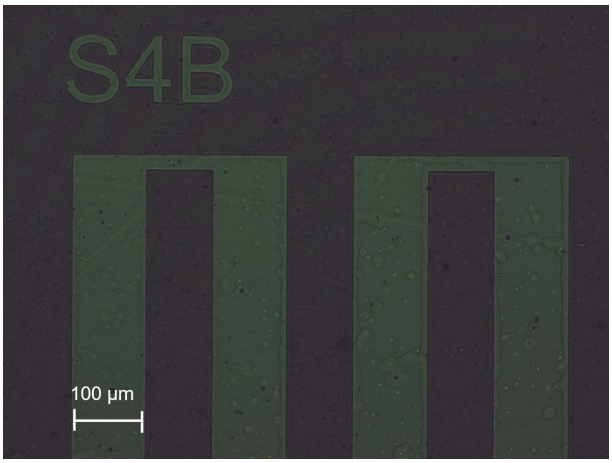

(a)

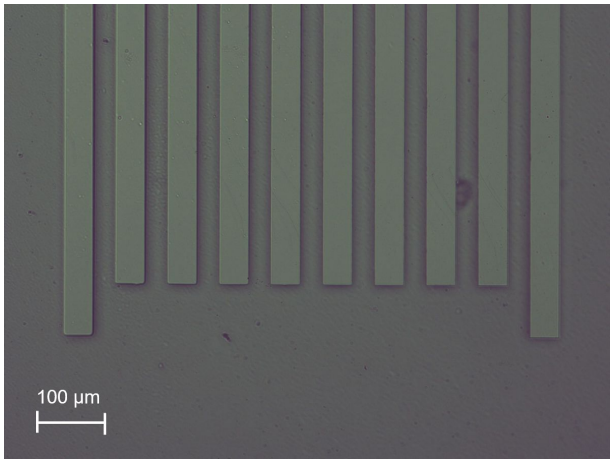

(b)

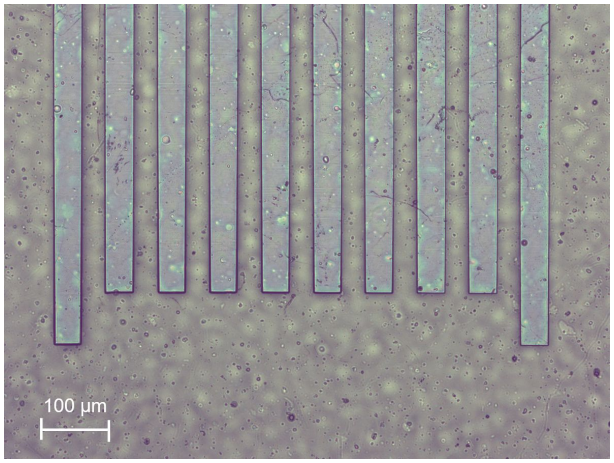

(c)

Figure 3.4: Optical microscope images of $Ni_{80}Fe_{20}$ samples after etching. (a) Sensor S4 in PI 125 µm; (b) Sensor S2 in PEN; (c) Sensor S2 in PI 25 µm.

3.2.1 Photoresist strip

As illustrated in Fig.3.1 (c), the etching step should be immediately followed by the photoresist strip, as the longer it stays on the sample, the more it hardens and becomes difficult to dissolve and remove. In order to do so, the sample is placed in a glass beaker and submerged in acetone for about 5 minutes. To help dissolve the PR faster, the container was manually agitated or placed in the ultrasounds for 2 to 3 minutes. When it seems that all PR has dissolved from the sample surface, the sample is rinsed with IPA (isopropyl alcohol) and deionized water. Once again, the sample is observed with the help of the optical microscope to check if in fact all the PR has disappeared.

In figure 3.5a there's an example of incomplete striping of the PR, namely on the left stripe when compared to the one on the right which is already clean. When this occurs, the sample needs to return to acetone a few more minutes. Lastly, the first layer of a PEN sample can be seen in Fig.3.5b.

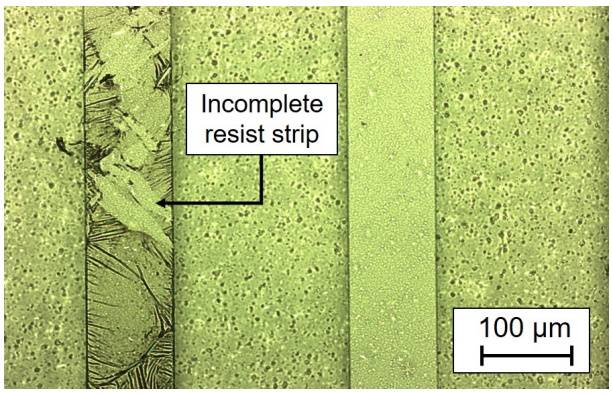

(a)

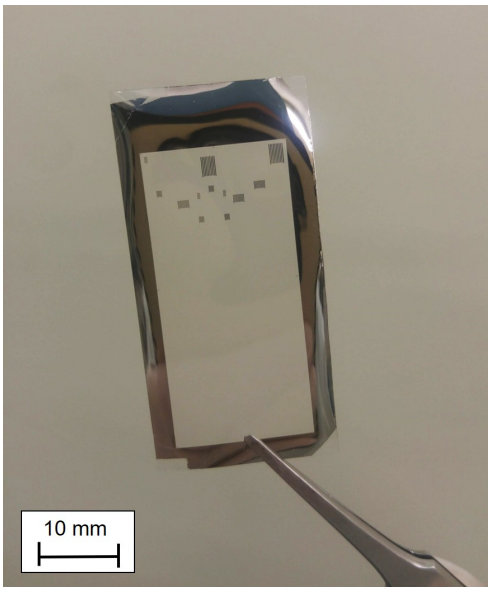

(b)

Figure 3.5: (a) Incomplete striping of photoresist on a $Ni_{80}Fe_{20}$ sample; (b) $Ni_{80}Fe_{20}$ sensors defined by etching on PEN substrate.

3.3 2nd lithography: electrical contacts

The second level of lithography is a non-inverted mask that defines the metal pads and leads that make the connections between sensors and the characterization acquisition system. The coating process was very similar to the first, but with the detail of making a pre-development (20 seconds) of the PR right after coating and prior to the lithography. This is mostly done in non-inverted layers that will further undergo a lift-off step, to improve the photoresist profile and facilitate its removal. Furthermore, when exposing a layer for lift-off, the amount of energy used is usually increased, and in this particular case it was 95% of 100 mW (maximum laser output power).

The second layer was only modified two times, as shown in Fig.3.6. In 3.6a the second layer corresponding to version 2 of the mask is showed although most of the pads are not visible due to the its size relative to the whole mask. The main difference between 3.6a and 3.6b is the shape of the contact leads: version 2 features right angle corners (3.6a) while version 3 (3.6b) has 45º junctions. Furthermore, as displayed in the detail figures for both versions, the contact pads size in 3.6b was increased in order to increase the probability of overlap between the first and second layer. The challenges that led to all alterations performed on the masks throughout the process will be explained in detail further on this chapter.

As depicted in Fig.3.1d, after lithography and development, the PR covers all the sample surface, except for the spots designed on the exposure where the photoresist dissolved. These spots will then be filled with metal to achieve electric contact. An example of a sensor after the second exposure is shown in Fig.3.7.

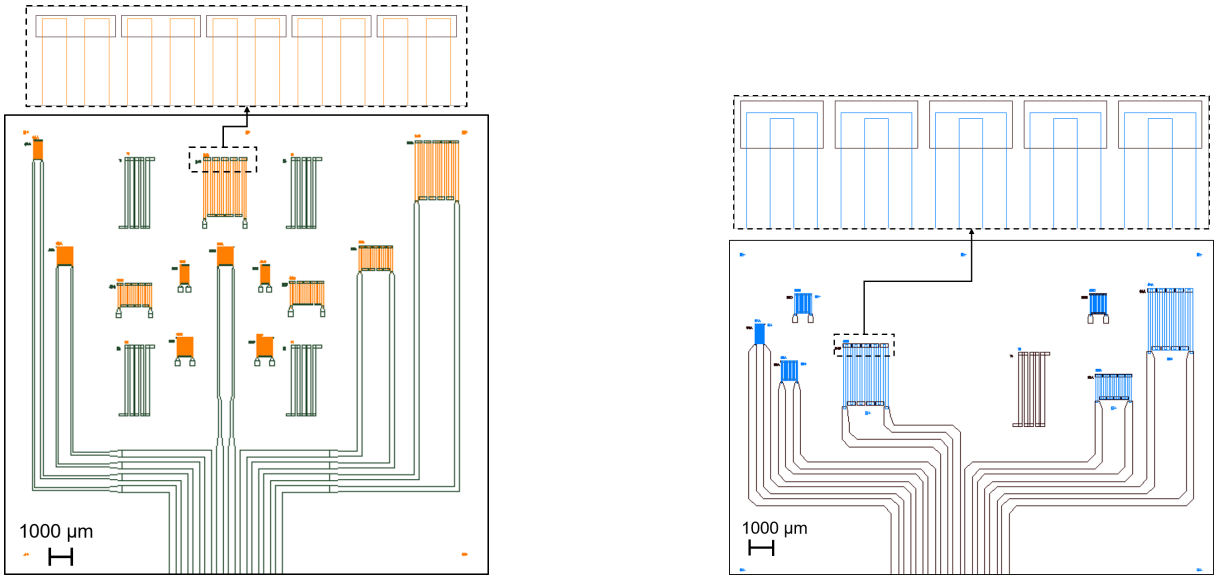

(a) (b)

Figure 3.6: Mask schemes: (a) V2 contact pads detail; (b) V3 contact pads details.

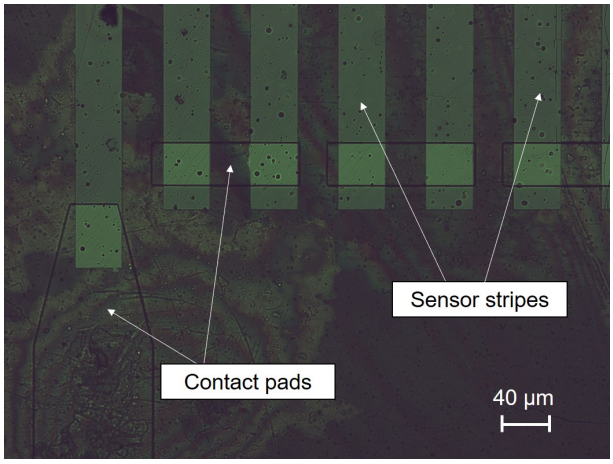

Figure 3.7: Example of sensor S2 after the second lithography.

3.4 Metallization and lift-off

To establish the electric contacts, a layer of metal (namely $Al_{98.5}Si_1Cu_{0.5}$) is deposited in Nordiko 7000, a multi-process system that features 4 chambers plus a dealer chamber. To perform this task only 3 of the 4 modules are used: module 2 does a sputter etch with Ar ions, which is used for a 30-60 seconds soft etch to clean the sample surface prior to metallization; Modules 4 is for depositing the $Al_{98.5}Si_1Cu_{0.5}$, which in this case was 3000 Å and module 3 was used for 100 Å TiW deposition that protects the contacts from oxidation. The depositions in N7000 are achieved through DC magnetron sputtering.

The power applied to the target during deposition is usually 0.5 kW but it had be decreased to 0.25 kW so the substrate doesn't suffer great temperature variations. In addition, the deposition of AlSiCu was made in a total of 6 $\times$ 500 Å steps with 5 cool down steps of 300 seconds between each deposition. The conditions are summarized in Table 3.4.

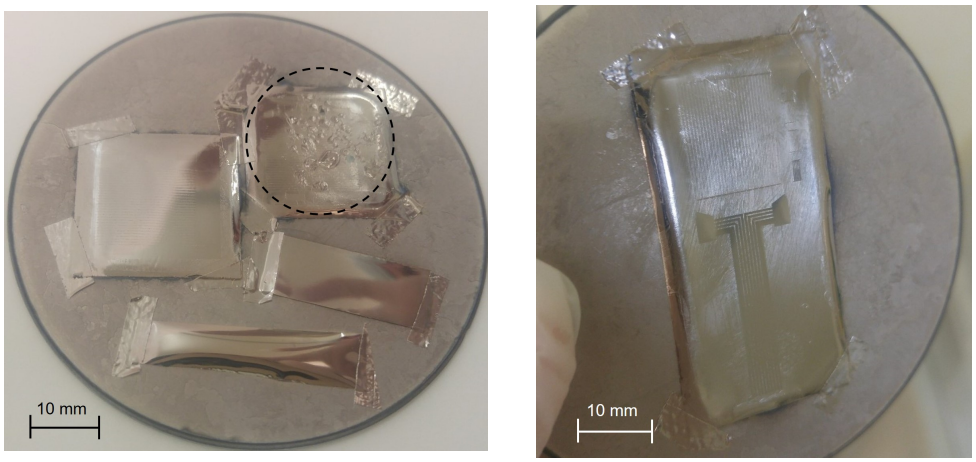

(a) (b)

Figure 3.8: Samples after metallization in N7000: (a) Test samples; Substrate of the highlighted sample on the right is PET while the left is PI-25; (b) Sample with the first version of the mask in PI-25;

In Figure 3.11 we can observe three examples of samples after metallization in N7000, where in fig. 3.8a the PET sample on the right has clear defects on the metal film, and afterwards during lift-off the sensor layer also peeled from the substrate. This is a strong indication that polyimide substrates handle temperature variations better.

Alternatively to N7000, in the last batch of samples the metallization step was made in a different machine.

Alcatel SCM 450 is also a magnetron sputtering machine, semi-automatic, as it is not controlable by software nor allows the creation of recipes with defined power and deposition times. It features 3 targets (2 RF and 1 DC) and 4 stations with sample holders and depositions can be performed in static or dynamic mode, with the samples rotating on top of the targets. Depositions must be stopped manually by rotating the shutter to a position between target and holder, and the plasma only stops by turning off the power supply. Despite these characteristics, this machine is suitable for quality thin film deposition with a chamber base pressure of 10^{-7} Torr and deposition pressures of around 10^{-3} Torr.

The metal available in this machine for depositing contacts is gold, with a buffer layer of chromium to improve adhesion. For this purpose, 100 Å Cr + 1000 Å Au were deposited with the conditions observed in Table 3.5. In fig. 3.9 samples after deposition in Alcatel are shown still in the proper machine holder.

Table 3.4: Deposition conditions in N7000.

Material	DC Power (W)	Voltage (V)	Current (A)	Gas flux (sccm)	Pressure (mTorr)	Rate (Å/s)
AlSiCu	0.22	327	0.8	49.9	3	4.8
TiW	0.25	395	0.64	49.6	3.2	2.5

Table 3.5: Deposition conditions in Alcatel.

Material	Power (W)	Bias (V)	Gas flux (sccm)	Pressure (mTorr)	Rate (Å/s)
Cr	20 (DC)	-	20	2.6	0.7
Au	20 (RF)	180	20	2.6	0.9

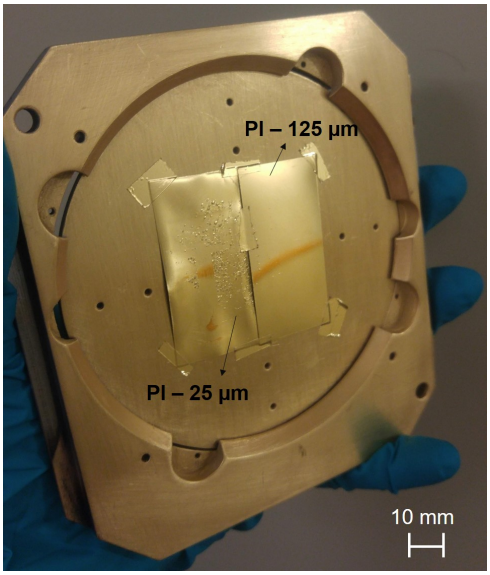

Figure 3.9: Samples after gold contacts deposition in Alcatel; Left sample is PI-25 substrate and right one is PI-125.

3.4.1 Lift-off

Lift-off is the last step of this process, and most times one of the most critical. When fabricating on rigid substrates, a commonly used reagent is Microstrip (as well as for PR strip) but as it requires a 65 ºC bath, it's not recommend for polymers. Instead, acetone is used once more to remove the photoresist and the excess metal on top. This step is very similar to the striping of photoresist after etch, but sometimes takes a little more time to remove everything. There's also an additional challenge with the 25 µm polyimide, as it rolls itself inwards when submerged in acetone for a couple of minutes, as it's shown in fig. 3.10. In this case, the lift-off is interrupted, the sample is cleaned with IPA and DI water to make it flat again, and then the process restarts. On average, the samples took 6 to 7 minutes to remove all the metal and photoresist, always with the help of ultrasounds. The main difficulty found during this step was being able to remove the excess metal from between contacts, since those are the spots in the sample where features are closest to each other. To give an example, between contact pads in the smaller sensors like S1 and S2 there's only a 10 µm distance, so these were the most problematic. Also, between the long contact leads, despite being 200 µm apart, in some samples this was also a challenge, as some metal would remain there after lift-off, short-circuiting the sensors. To solve this issue, a cotton bud impregnated with acetone was used to try and remove the metal from those spots, scratching the zone very lightly. For most of the samples where this was performed it worked well, removing the metal unreachable with lift-off, but there were a few samples where it was fatal for the sensors, as they came off because of the applied force on the surface. An example is shown in Fig.3.12, where the PEN sample

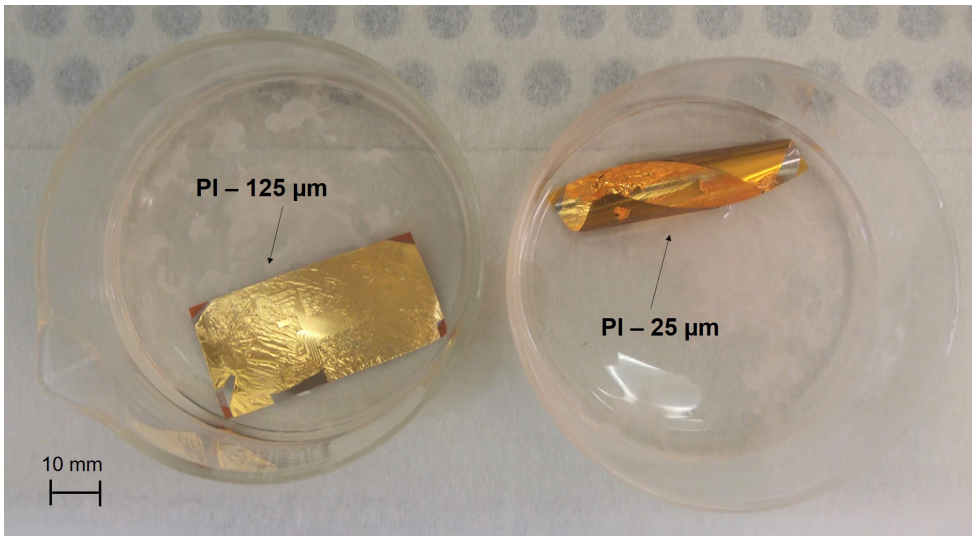

Figure 3.10: Samples with gold metallization from Alcatel in lift-off process; Sample on the left is PI - 125 and on the right is PI - 25.

on the right has the contacts scratched from the substrate, making it inappropriate for measuring.

3.5 Fabrication challenges and mitigation

Fabricating on flexible substrates is a challenge, as the established techniques for silicon and glass are not the most indicated and need adaptations. In addition to changes already described above, such as using acetone to dissolve the PR instead of microstrip or a different holder during lithography, there were more technicalities that will be explained in this section.

The first obstacle appeared on the coating step of the samples. When performing the lithography of the first sample, film cracks were visible in the laser camera. After the lithography process, the sample was inspected in the optical microscope and the defects were visible (Fig. 3.13). The fabrication of the sample proceeded and when trying to measure the magnetic transport we came to the conclusion that

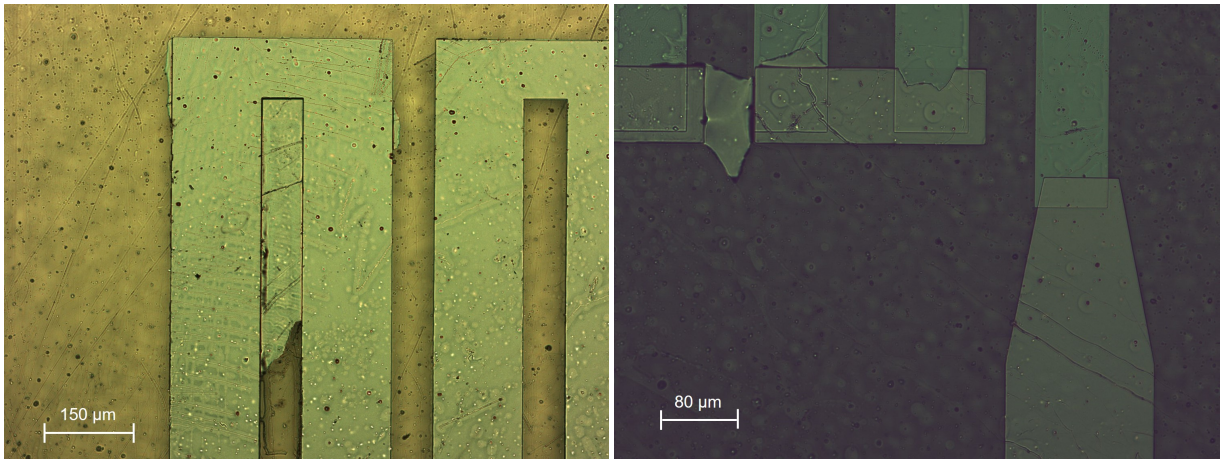

(a) (b)

Figure 3.11: Lift-off defects: (a) AlSiCu test feature; (b) Sensor in a PI-25/$Co_{90}Fe_{10}$ alloy sample.

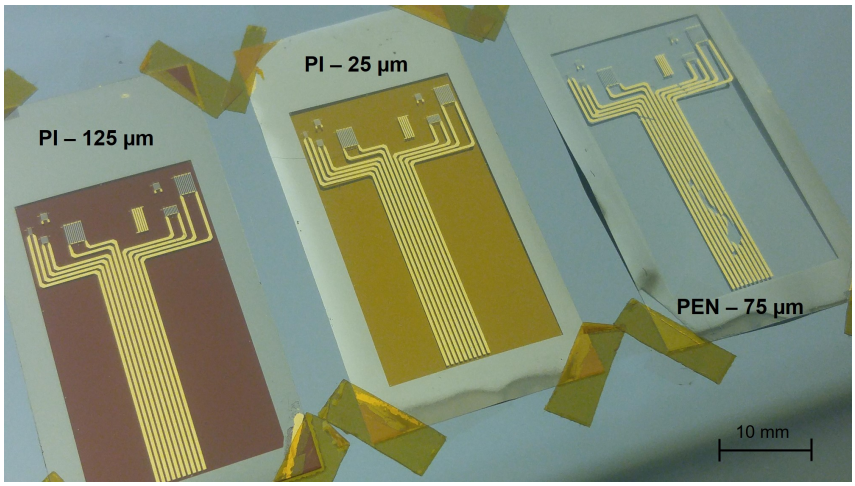

Figure 3.12: Finished samples on the three different substrates attached to a wafer for optical inspection.

it was open circuited. After some tests it was seen that in fact, if the cracks cross the majority of the sensor stripes, electric current is unable to flow through the sensor.

The samples were also observed in a SEM at INESC-MN, which is a Raith-150 system, consisting of an electron-beam lithography tool converted from a LEO 1500 series scanning electron microscope. It integrates the thermal field emission filament technology, with a nominal resolution of 20 nm and capable of processing up to 8 inch wafers [19]. In fig. 3.14 some acquired photos of the cracking are shown.

Possible causes were weighted, and one of the factors influencing these defects might be the thermal expansion coefficients (CTE) mismatch between polymer and metal. When joining two materials, this property has to be taken into account during cooling processes, because it will induce tensile stress in one material and compressive stress in the other [48]. The CTE of polyimide is around 20×10^{-6}/K while for $Ni_{80}Fe_{20}$ alloy, in a percentage close to ours, it is around 12×10^{-6}/K [49]. This implies a coefficient ratio of around 1.7 between the two materials, meaning that polyimide expands 1.7 times more than NiFe with the same amount of heating.

Measures were taken towards mitigating this issue, including promoting a slow cooling of the sample after the photoresist bake at 85 °C; in the development, the baking step at 110 °C was also adapted

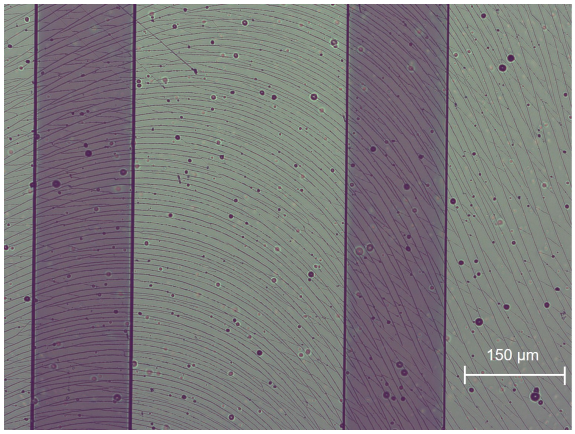

Figure 3.13: First sample fabricated, with cracks visible after the first layer lithography.

to 85 °C. Adopting these changes, the sample mask was modified to include 5 sensors with different sizes, at it was shown above. As it's possible to observe in the mask layout (see fig. 3.6b), 4 sensors are located on the peripheral region to try to minimize the cracks, as it was observed during heating of the samples that the middle region suffers more induced stress from the temperature variations.

There's also an important aspect to consider: this micro-cracking phenomena was only observed in the films deposited on the thinnest polyimide (25 µm). The Stoney formula [50] presents a good explanation for this, which is the fact that the radius of curvature of substrate plus film increases with the square of the substrate thickness. This means that, considering the same amount of stress generated during deposition, the samples with PI-125 µm and PEN-75 µm have a larger radius of curvature, implying less bending of the sample. Upon heating, for example in the baking steps, the thermal stress will contribute to increase the residual stress of the substrate, thus decreasing the radius of curvature and causing the thin film to crack.

$$R_{s+f} = \frac{1}{6\,\sigma_s\,t_f}\frac{E_s\,t_s^2}{1-\nu} \tag{3.1}$$

where R is the radius of curvature of the substrate and thin film structure, σ_s, E_s, t_s are the stress, Young's Modulus and the thickness of the substrate and t_f is the thickness of the film.

After fabricating a few samples, it was clearly observed that the bigger sensors S3 and S4 had notably more cracks that S1 and S2, however, we still were able to measure more AMR curves in these sensors than in the smaller.

Finally, the last version of the sensors was achieved in a mask that did not have a sensor in the middle region, as this had suffered severely more cracks than any other sensor during fabrication.

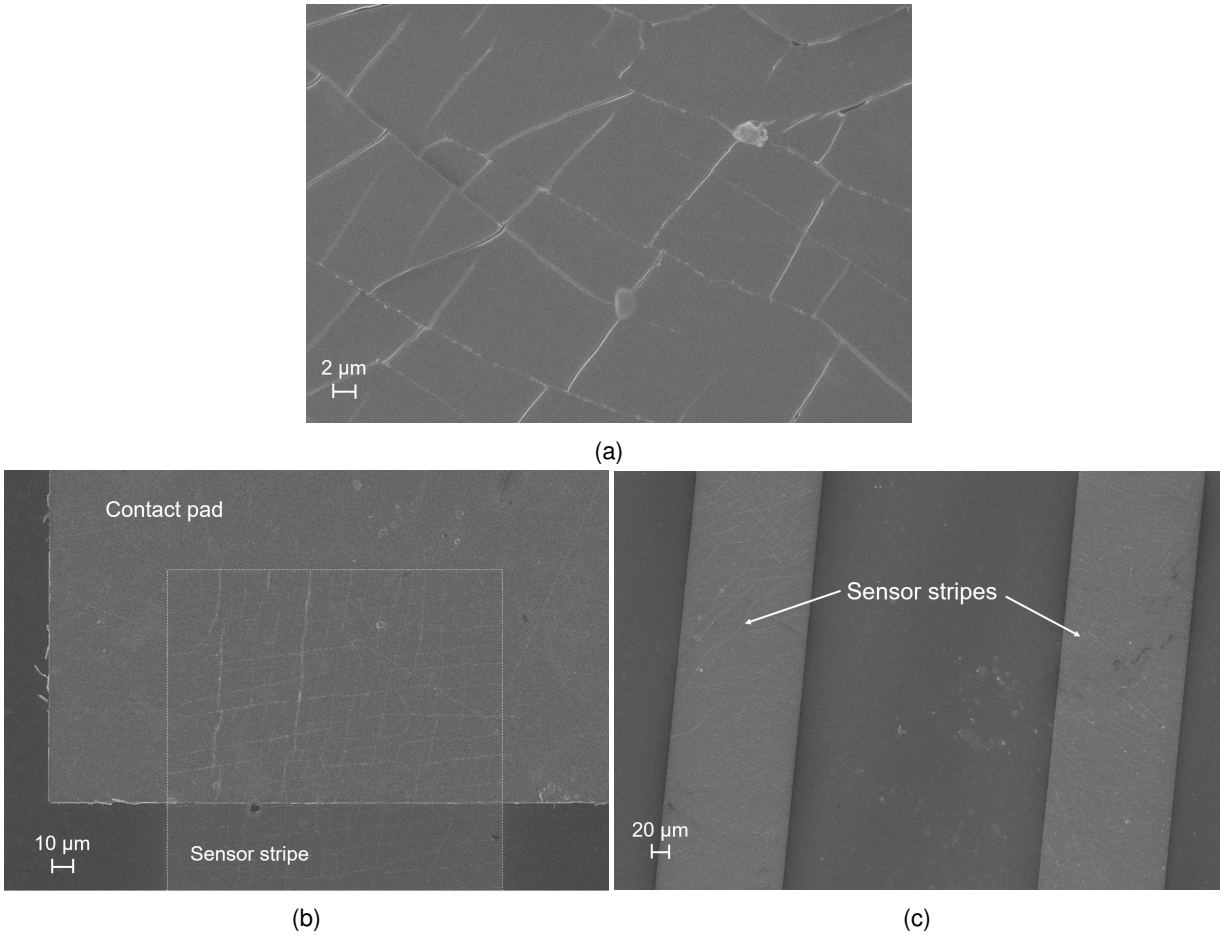

Figure 3.14: SEM images of $Ni_{80}Fe_{20}$ and $Co_{90}Fe_{10}$ samples fabricated on PI - 25: (a) $Co_{90}Fe_{10}$ alloy sample; (b) $Ni_{80}Fe_{20}$ alloy sample, junction between sensor and contact pad; (c) $Co_{90}Fe_{10}$ alloy sample, sensor stripes.

Chapter 4

Device characterization: results and discussion

4.1 Assembly of bending setup

The samples in this work were designed to be directly connected to a printed circuit board (PCB) for structures characterization. Since the main scope of this analysis was to measure bent samples, an alternative solution to the conventional micro-probes had to be developed. Magnetic characterization at INESC-MN is perfomed on a setup (Fig.4.1) comprising a Keithley 220 programmable current source, a Keithley 182 digital voltmeter, microscope, 4 micro-probes, and two coils capable of generating a field up to 140 Oe (14 mT).

Instead of the probes, samples are inserted in a flex cable connector (Fig.4.2c), which in turn was

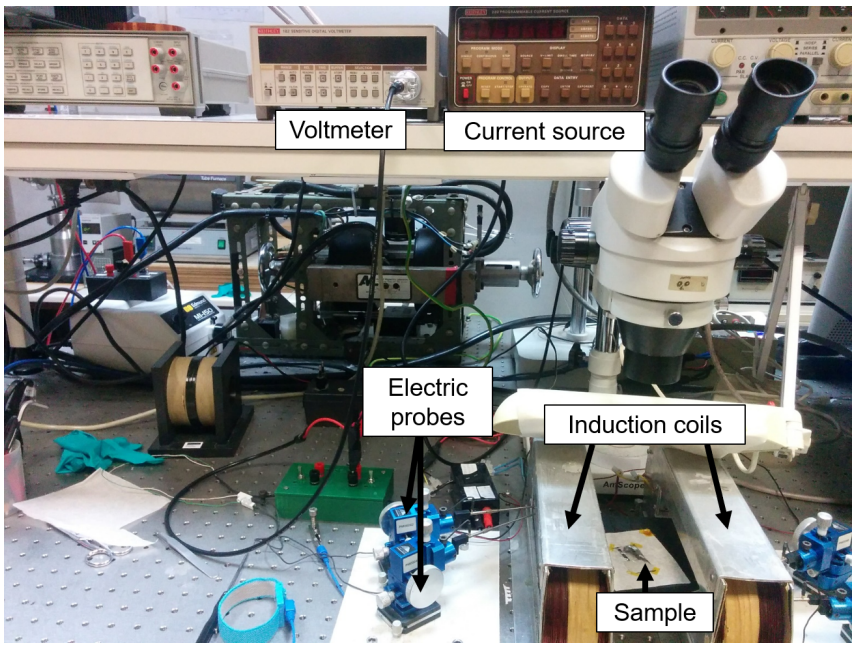

Figure 4.1: Sensor transfer-curve measurement setup installed at INESC-MN.

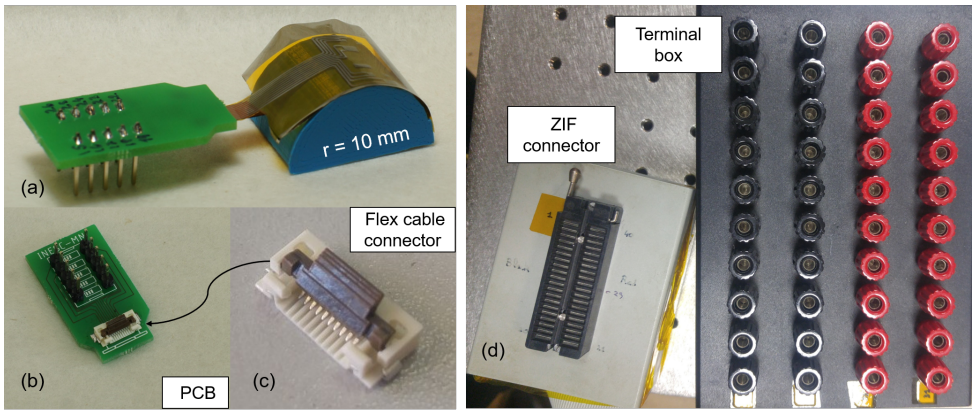

Figure 4.2: Components of the bending characterization setup: (a) Sample bent and inserted on the PCB connector; (b) PCB; (c) Flex cable connector; (d) ZIF connector and terminal box.

soldered to a PCB designed especially for this work (Fig.4.2b). In Fig.4.2a there is an example of a sample connected to the PCB and bent on one of the bending supports. These were 3D printed with different radii of curvature, namely 2.5, 10 and 12 mm.

It is important to highlight that the design of the samples mask was elaborated in accordance with this flex cable connector, which has 10 pads, so each sample has 5 sensors (each has 2 metal leads that fit exactly on top of the connector pads). The PCB was then designed to have also 10 leads and each pair of pins is connected to one sensor.

To integrate this assembly on the existing setup, the PCB is inserted in a ZIF (zero insertion force) connector attached to a terminal box (Fig.4.2d). This is shown in Fig.4.3, where a sample is mounted on the smallest bending support (2.5 mm radius); the setup is placed between the two coils for characterization. The connections between sensor and acquisition system are made through the terminal box with cables. This system also helps to prevent the sensors from cracking, as it allows to choose the sensor to measure on the terminal box without actually touching the sample. This is an advantage when working with flexible substrates, as handling of the sample may lead to a decrease in performance of the sensors.

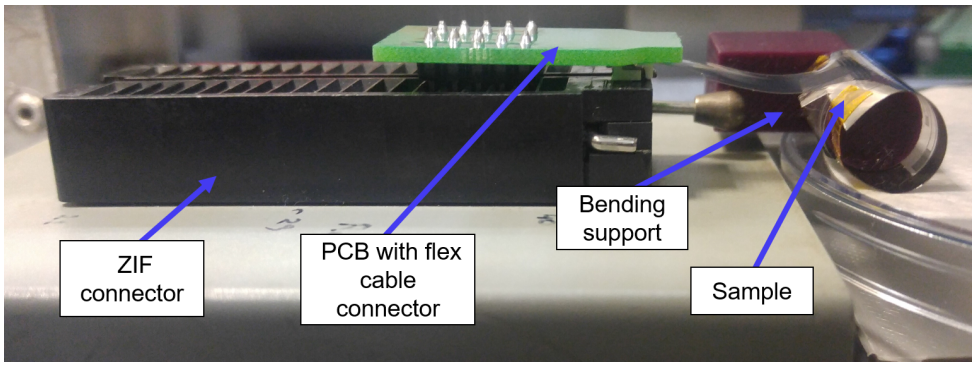

Figure 4.3: PCB inserted in the ZIF connector, with a sample mounted in a bent mode ready for measurements.

4.2 Anisotropic Magnetoresistance curves

The most important tool for characterizing the behavior and performance of a magnetoresistive sensor is a magneto-transport curve. The relevant parameters are the minimum and maximum resistance (R_{min} and R_{max}), which define the AMR ratio, as well as the saturation field, which is intrinsically related to the effective magnetic anisotropy. These curves have a bell shape, as discussed in Chapter 2, and display the resistance or AMR ratio as a function of the applied magnetic field.

To obtain these curves, a sample is placed between the Helmholtz coils, which in turn generate a variable magnetic field. Measures were performed from - 14 to 14 mT, with a current bias to the active AMR sensor of 1 µA. Field steps were not constant throughout the whole measurement: from -14 to -4 the step was 2 mT, from -4 to 4 it was 0.4 mT (in order to increase resolution in this zone) and increases to 2 mT again until 14 mT. H_{sat} refers to the field at which the magnetization is saturated along the direction of the external applied field. Fig.4.4 shows a layout of the characterization, where H_{app} is the applied field, M and M' are the initial magnetization direction and the magnetization rotation with the field.

Measurements were performed in sequence as illustrated in Fig.4.5. Each sample has 5 sensors, all of them were first tested for output signal, and then to obtain a transport curve. The curves that depicted the best electrical signal and shape were chosen to discuss further the representative magnetic and transport behavior.

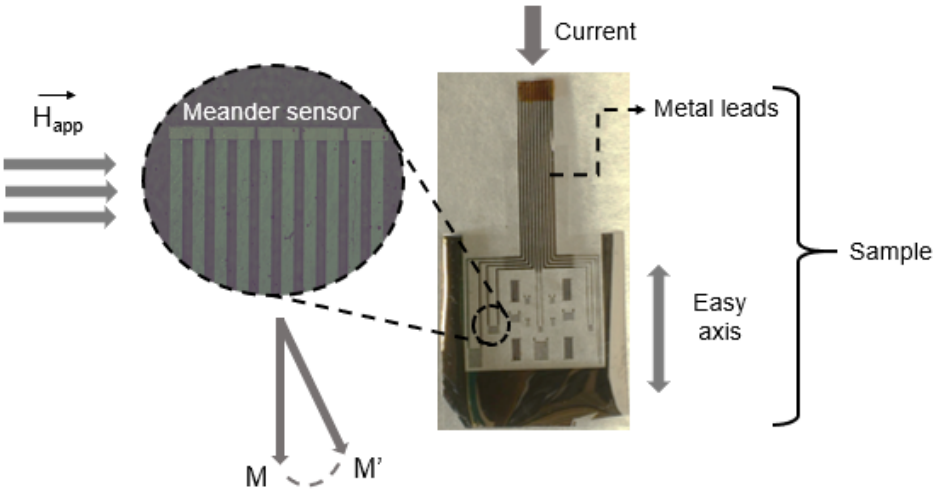

Figure 4.4: Characterization layout: H_{app} is the applied field, M and M' are the initial magnetization direction and the magnetization rotation with the field. The image shows a sample with a sensor close-up.

Figure 4.5: Measurements with bending sequence flowchart.

4.2.1 $Ni_{80}Fe_{20}$ curves

$Ni_{80}Fe_{20}$ was measured on the three substrates. The sample on PI-125 µm was not measured with r_{bend} = 2.5 mm due to handling difficulties caused by the stiffness of the substrate. In Fig.4.3 there is an example of the $Ni_{80}Fe_{20}$ sample on PEN bent to 2.5 mm radius, and this can also be seen in detail in Fig.4.7. Regarding the AMR signal, the typical values for films on silicon substrates go up to 2% [51], and on flexible substrates studies report that this value is around 0.6 to 1% [52].

Starting by comparing the curves without any bending (Fig.4.6 and first plot in all samples), there is a clear evidence that PI-125 µm is the substrate that yielded the highest AMR ratio, with values around 0.9%, very close to values obtained in rigid substrates. Looking at the measured resistance, we can see that the values are around 4000 Ω for the three substrates, and since the measured sensors have different sizes, they also had different nominal resistances. The sensor on PI-125 µm showed the smallest resistance increase comparing to the nominal value, which indicates that it did not deteriorate during fabrication as much as the sensors on other substrates, presenting less defects such as micro-cracking. Regarding the saturation field, PI-25 µm presents the smallest value (1.6 mT), followed by PEN-75 µm (2.2 mT) and PI-125 µm (2.3 mT).

Both AMR signal and H_{sat} values seem to be stable even with increased curvature. Only on PI-25 µm a reduction in signal is observable, especially with r_{bend} = 2.5 mm. The signal decrease was accompanied by an increase in resistance, probably due to sensor degradation after several bending cycles. The saturation field appears to be more sensitive on PI-125 µm, where a slight broadening of the curve happens with the consecutive bending, thus increasing H_{sat}. On PI-125 µm it is observable that the ascending and descending curves are shifted, and this can be quantified by a switching field (H_{sw}),

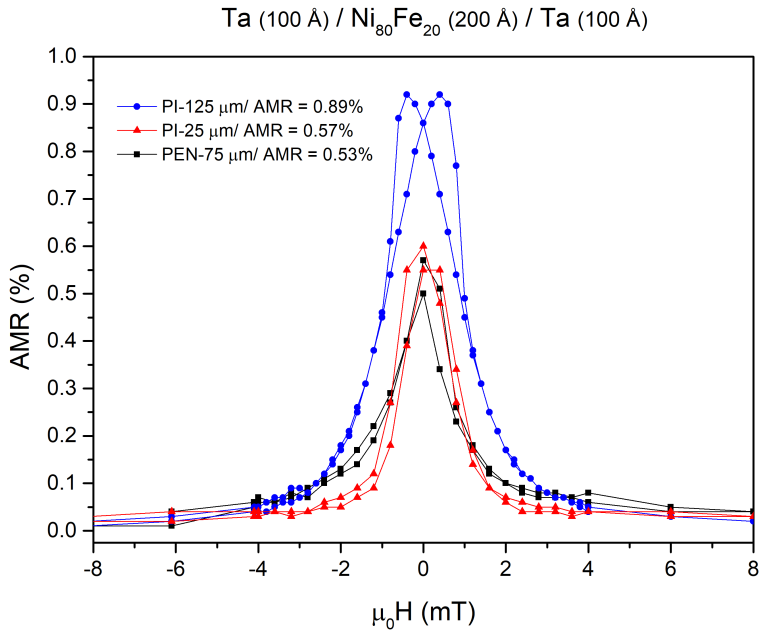

Figure 4.6: Ta 100 Å /$Ni_{80}Fe_{20}$ 200 Å/ Ta 100 Å // on the three substrates AMR curves measured on flat mode (r = ∞).

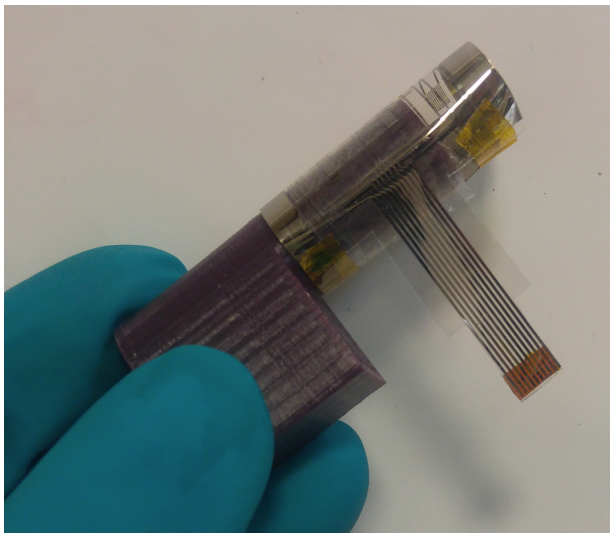

Figure 4.7: $Ni_{80}Fe_{20}$ sample on PEN bent on 2.5 mm radius support.

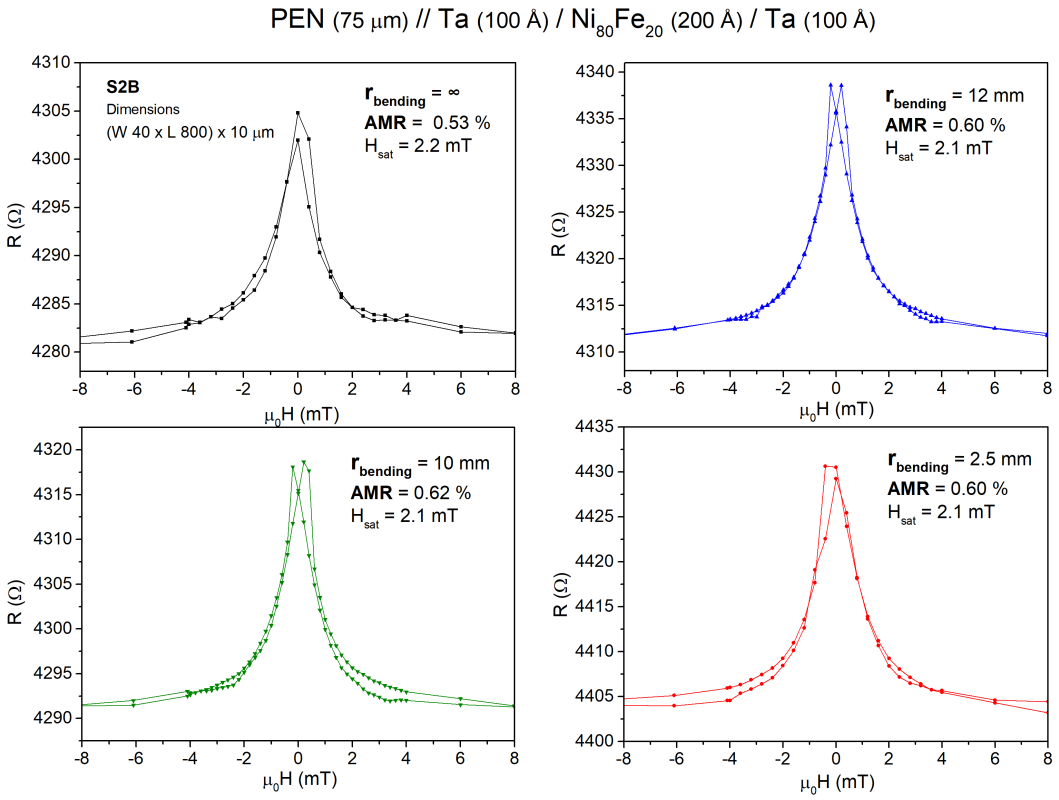

Figure 4.8: Ta 100 Å /$Ni_{80}Fe_{20}$ 200 Å/ Ta 100 Å // PEN μm AMR curves measured on flat mode (r = ∞), bending #1, #2 and #3.

in this case of 0.4 mT. This shift is due to the easy axis induced during deposition being tilted relatively to the current direction. A possible source for this is the internal stress during deposition or a geometrical misalignment.

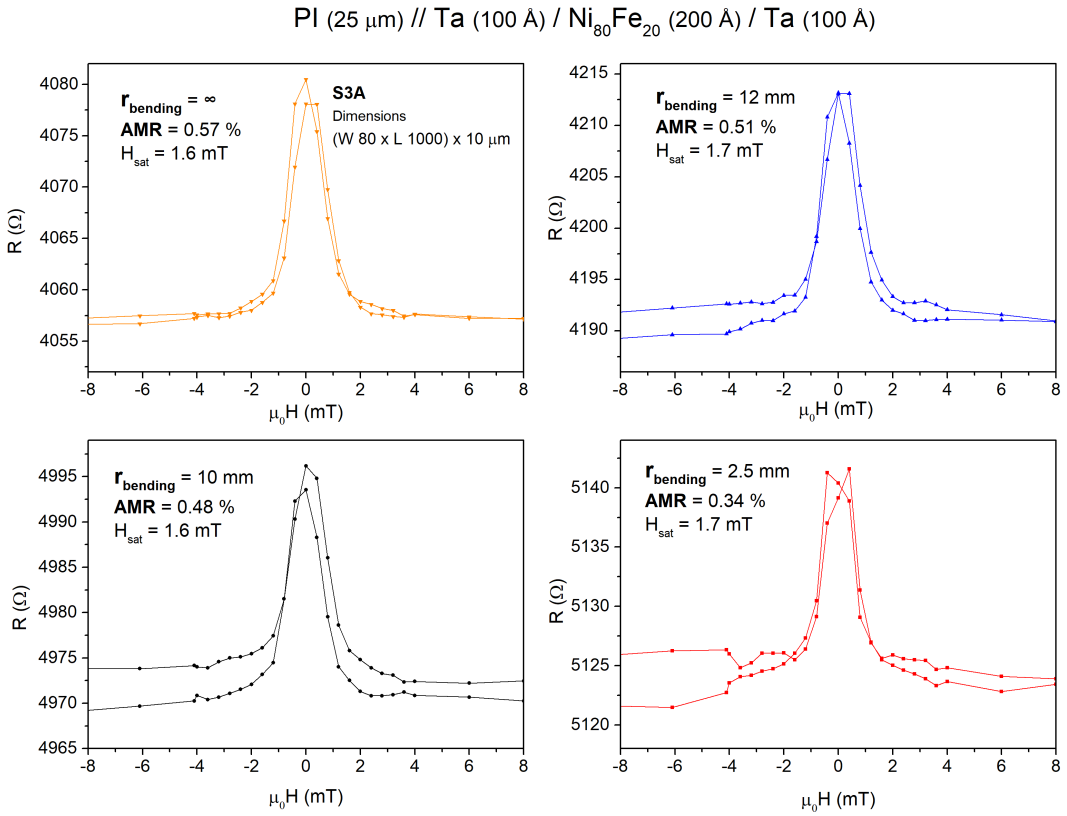

Figure 4.9: Ta 100 Å /$Ni_{80}Fe_{20}$ 200 Å/ Ta 100 Å // PI-25 µm AMR curves measured on flat mode (r = ∞), bending #1 and #2 and #3.

4.2.2 $Co_{90}Fe_{10}$ curves

Regarding $Co_{90}Fe_{10}$ samples, it was not possible to measure this film on PEN, nor with r_{bend} = 2.5 mm. The curves on PI-25 µm present a very low AMR ratio. Literature reports AMR signals for CoFe alloys around 0.5 to 0.55% [53]. The presented values for H_{sat} are a rough estimate, as the curves shape does not allow a very precise estimation, but looking at the curves, this value seems to be constant with increased bending. Furthermore, they are significantly higher than the saturation values of $Ni_{80}Fe_{20}$, as expected. On PI-125 µm, the first two curves without bending refer to 2 different sensors; the first is a test sensor, meaning that it was measured with the micro-probes instead of the flex cable connector, while the second curve is from one of the 5 main sensors that connect to the PCB. Although their shape is very similar, S4B showed a considerable increase in resistance, as compared to the testing counterpart. This is probably due to degradation of the conductive metal leads, which in turn led to a loss of AMR signal. The curve with r_{bend} = 10 mm shows a further reduction of this output and increase in resistance. Also, this curve did not reach saturation even at 14 mT.

4.2.3 Anisotropy contributions and influence on sensor behavior

As discussed in Chapter 1, there are different sources of anisotropy that influence the system. As stated earlier, H_{sat} is the field required to saturate the magnetization, and in order for this to happen, this

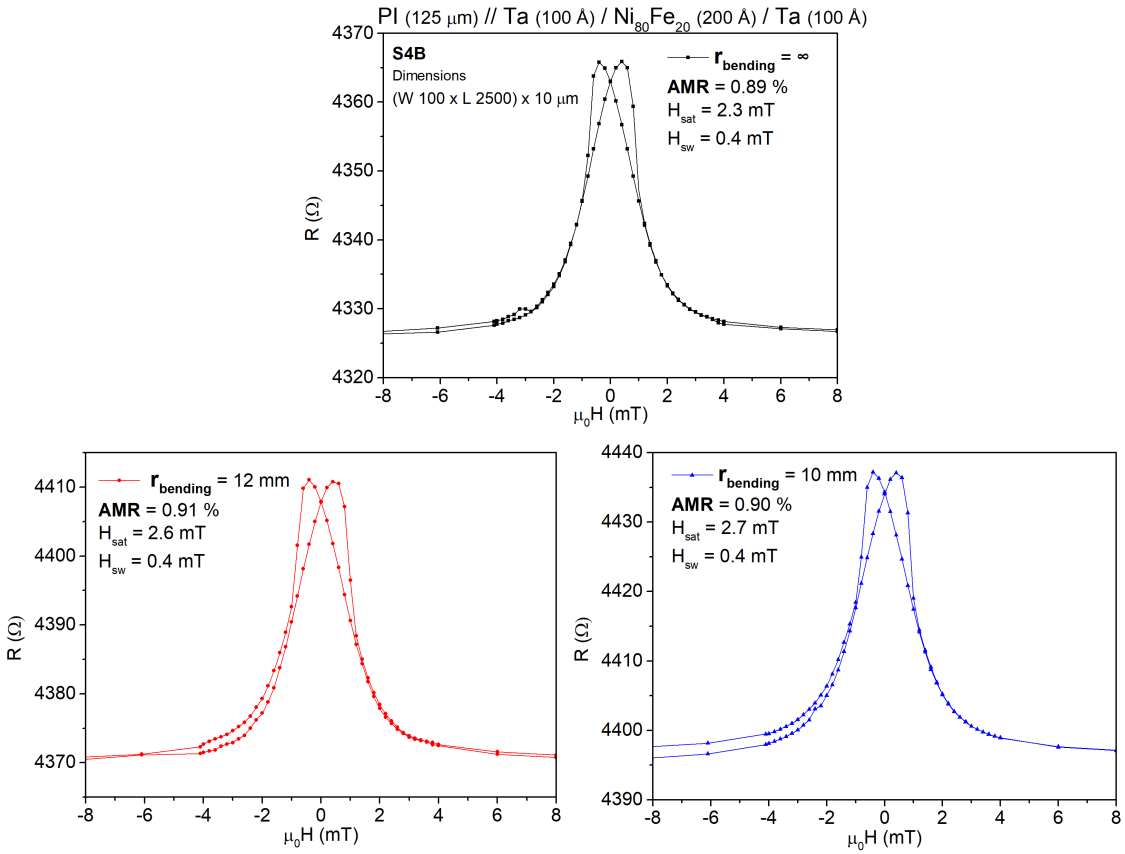

Figure 4.10: Ta 100 Å /$Ni_{80}Fe_{20}$ 200 Å/ Ta 100 Å // PI-125 µm AMR curves measured on flat mode (r = ∞), bending #1 and #2.

field has to overcome the total anisotropy of the system, which makes magnetization lie along a certain direction.

When the thin film is patterned, shape anisotropy is no longer negligible and the demagnetizing field is an important factor that can be estimated to understand its influence on the total anisotropy. This depends on sample shape, namely the thin film thickness and the width of the structure. The length is assumed to be infinite. The demagnetizing field can then be estimated through Eq. 4.1:

$$H_{dem} = 4\pi M_s \frac{t}{w} (CGS) \tag{4.1}$$

where H_{dem} comes in CGS units (Oe), M_s is the saturation magnetization (same value used in Chapter 2), t is the ferromagnetic thickness (200 Å) and w is the width of the sensor stripe. The results for each sample are presented in Table 4.1 in SI units.

The smaller the sensor width and the larger the magnetization value, the more pronounced this phenomenon is. In the case of this work, the demagnetizing field contributes to anisotropy, but it is not the dominant factor, since it is estimated to vary from 0.3 to 0.5 mT through all the samples, but the minimum saturation field measured is 1.6 mT.

Induced stress through bending is a crucial aspect to be considered. This parameter can be calculated through an equation deriving from the isotropic Hooke's law (Eq. 4.2):

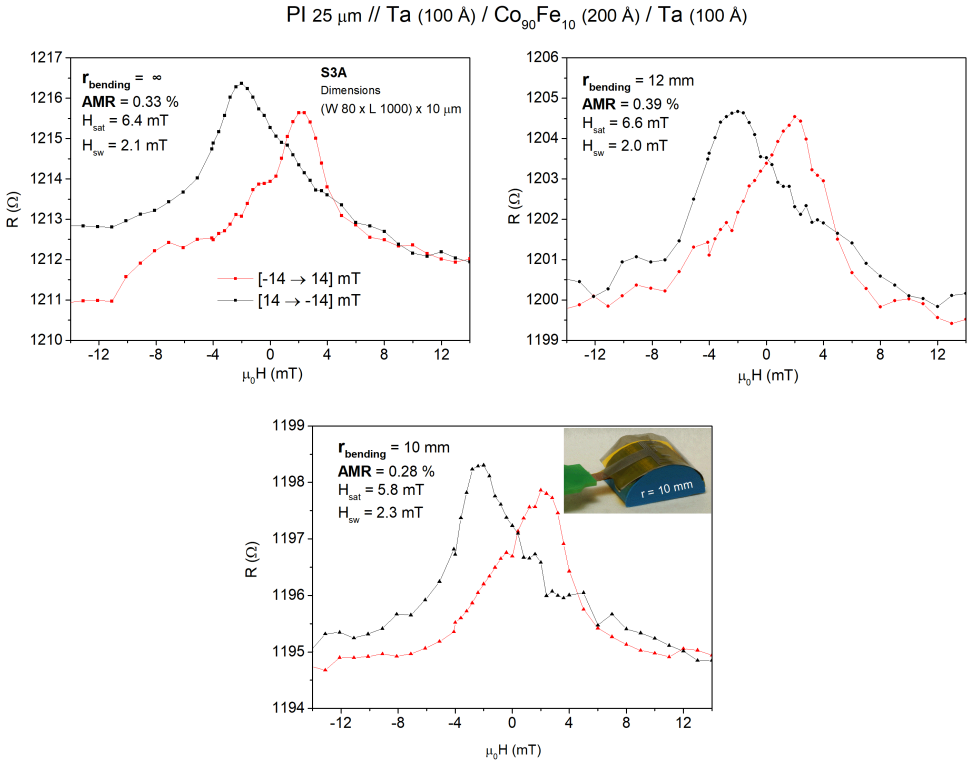

Figure 4.11: Ta 100 Å /$Co_{90}Fe_{10}$ 200 Å/ Ta 100 Å // PI-25 μm AMR curves measured on flat mode (r = ∞), bending #1, #2.

$$\sigma_u = E_f \left(\frac{t_f + t_s}{2R}\right) \frac{1 + 2\frac{t_f}{t_s} + \frac{E_f}{E_s}\frac{t_f^2}{t_s^2}}{\left(1 + \frac{t_f}{t_s}\right)\left(1 + \frac{E_f}{E_s}\frac{t_f}{t_s}\right)} \tag{4.2}$$

where E_f, E_s are respectively the film and substrate Young's modulus, t_f, t_s are respectively the film and substrate thicknesses and R is the radius of curvature at which the sample is bent [54]. The values for the Young's modulus of the films were taken from Ref. [54]. For $Co_{90}Fe_{10}$ thin film, E was assumed to be the same as for $Ni_{80}Fe_{20}$ (180 GPa). The stress was calculated for each curvature radius at which the samples were subjected and the results are presented in Table 4.1 in MPa. These values are in accordance to literature for stress values on thin films [55]. Since the thin film properties were considered to be the same (thickness and Young's modulus), the substrate plays an important role in these estimations. Both polyimide substrates have the same E_s, so it is visible that a difference of 100 μm in thickness has a critical impact on the final stress of the sample. For example, for a curvature radius of 10 mm, PI-25 μm yields a stress of 54 MPa, whistle PI-125 μm displays a stress of 549 MPa. When applying a bending of 2.5 mm, the stress on the sample also increases by a factor of 4, comparing to r_{bend} = 10 and 12 mm.

It is possible to estimate the anisotropy constant, $K_{u\sigma}$, generated by stress:

$$K_{u\sigma} = \frac{3}{2}\sigma\lambda_s \tag{4.3}$$

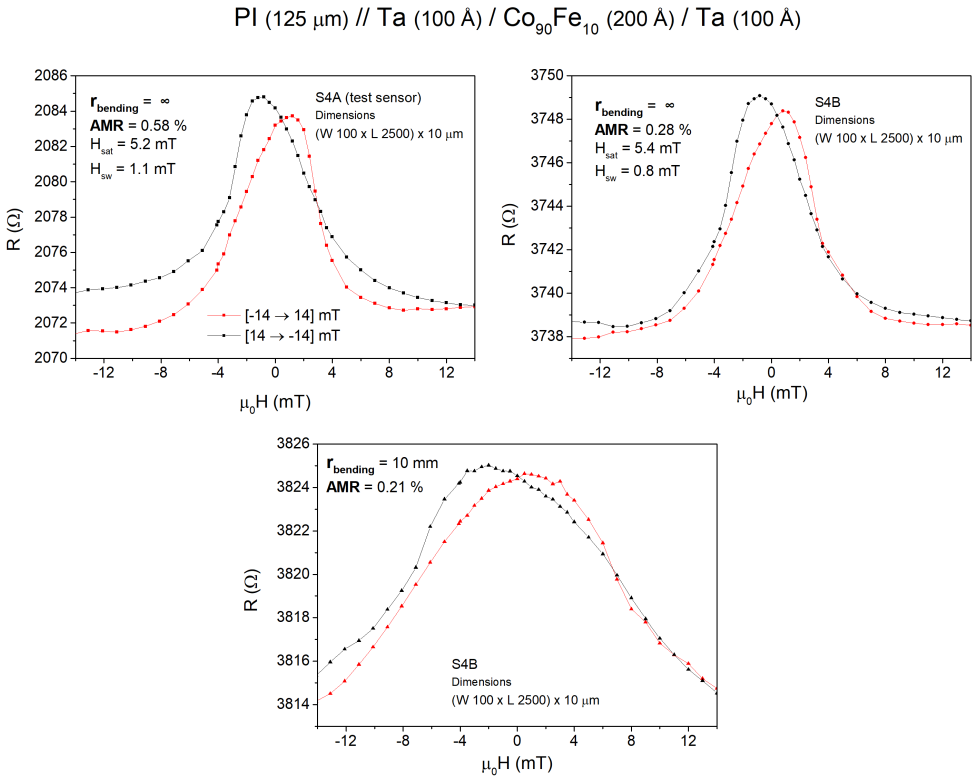

Figure 4.12: Ta 100 Å /$Co_{90}Fe_{10}$ 200 Å/ Ta 100 Å // PI-125 μm AMR curves measured on flat mode (r = ∞) (two sensors) and bending #2.

The values for the magnetostriction coefficient were considered to be λ_s = 0.75×10^{-6} for $Ni_{80}Fe_{20}$ [54] and λ_s = 3.58×10^{-6} for $Co_{90}Fe_{10}$ [56]. Since the magnetostriction coefficients for these alloys are low, the values of the magnetoelastic anisotropy are also small; however they are in the expected range [17].

Finally, the field associated with the induced stress is calculated according to Eq. 4.4:

$$H_\sigma = \frac{2K_{u\sigma}}{\mu_0 M_s} \tag{4.4}$$

The values are all summarized in Table 4.1.

Looking at the results, it follows that in $Ni_{80}Fe_{20}$ samples on PEN-75 μm and PI-125 μm, H_σ has a strong contribution to the saturation field, as these values are in the same order of magnitude and are considerably larger than H_{dem}. This stress comes from the substrate thickness, and although $Ni_{80}Fe_{20}$ has near zero magnetostriction, when deposited on these substrates the stress influence is not negligible. The same does not hold for PI-25 μm, where both anisotropies contribute almost equally on both ferromagnetic alloys.

$Co_{90}Fe_{10}$ results are somewhat different, as seen that its saturation field on both substrates has a greater discrepancy from H_{dem} and H_σ. On PI-125 μm it was not possible to estimate H_{sat} because with the field of 14 mT the saturation of magnetization was not reached, meaning that H_σ = 3.7 mT is a very small contribution. This is probably due to the magnetocrystalline anisotropy of $Co_{90}Fe_{10}$ being

more determining in the total anisotropy when compared to $Ni_{80}Fe_{20}$.

Table 4.1: Magneto-transport properties of the patterned samples with 200 Å of sensing layer encapsulated with 100 Å Ta. AMR (%) is the anisotropic magnetoresistance ratio, H_{sat} is the saturation field and H_{sw} the switching field extracted from the curves. H_k is the anisotropy field estimated from the VSM hysteresis loops. H_{dem}, σ, $K_{u\sigma}$ and H_σ were calculated from several parameters. For each sample, the values correspond to the same sensor, except for Ta /$Co_{90}Fe_{10}$/ Ta // PI-125, in which it was not possible to measure for more bending radius and instead, 2 sensors are present with r = ∞.

Sample	$r_{bending}$ (mm)	AMR (%)	H_{sat}^{curve} (mT)	H_{sw}^{curve} (mT)	H_k^{vsm} (mT)	$H_{dem}^{calc.}$ (mT)	$\sigma^{calc.}$ (MPa)	$K_{u\sigma}^{calc.}$ (J/m^3)	$H_\sigma^{calc.}$ (mT)
Ta 100 Å/$Ni_{80}Fe_{20}$ 200 Å/ Ta 100 Å // PEN	∞	0.53	2.2	-	0.7	0.5	-	-	-
	12	0.60	2.1	-	-		310	348	0.8
	10	0.62	2.1	-	-		372	418	1.0
	2.5	0.60	2.1	-	-		1490	1670	4.0
Ta 100 Å/$Ni_{80}Fe_{20}$ 200 Å/ Ta 100 Å // PI-25	∞	0.57	1.6	-	0.5	0.3	-	-	-
	12	0.51	1.7	-	-		45	51	0.1
	10	0.48	1.6	-	-		54	61	0.2
	2.5	0.34	1.7	0.4	-		216	243	0.6
Ta 100 Å/$Ni_{80}Fe_{20}$ 200 Å/ Ta 100 Å // PI-125	∞	0.89	2.3	0.4	0.7	0.2	-	-	-
	12	0.91	2.6	0.4	-		458	515	1.2
	10	0.90	2.7	0.4	-		549	618	1.5
Ta 100 Å/$Co_{90}Fe_{10}$ 200 Å/ Ta 100 Å // PI-25	∞	0.33	6.4	2.1	5.5	0.5	-	-	-
	12	0.39	6.6	2.0	-		45	241	0.3
	10	0.28	5.8	2.3	-		54	290	0.4
Ta 100 Å/$Co_{90}Fe_{10}$ 200 Å/ Ta 100 Å // PI-125	∞ (S4A)	0.58	5.2	1.1	3.9	0.4	-	-	-
	∞ (S4B)	0.28	5.4	0.8	-		-	-	-
	10	0.21	-	-	-		549	2950	3.7

Chapter 5

Conclusions and future work

This dissertation focused on the fabrication and characterization of magnetic sensors based on anisotropic magnetoresistance onto three flexible substrates. Two alloys ($Ni_{80}Fe_{20}$ and $Co_{90}Fe_{10}$) were deposited with different intrinsic magnetic properties and the impact of the substrate on their final behavior was evaluated using different characterization techniques.

Resistivity measurements displayed consistent values with literature and previous works done at INESC-MN. X-ray diffraction analysis of PEN and $Ni_{80}Fe_{20}$ revealed highly textured materials with a single highly preferred crystallographic orientation, respectively and using Miller indices notation, (-110) and (111), which correspond to average interplanar distances of 3.40 Å and 2.03 Å.

A study of magnetic properties of as-deposited films was also performed. The results obtained for H_{sat} and H_c are consistent with literature and among samples of the same alloy in different substrates. As expected, $Co_{90}Fe_{10}$ has higher coercive and anisotropy fields than $Ni_{80}Fe_{20}$, and therefore the estimated anisotropy constant is also higher for this material.

Three mask versions were designed to optimize the sensors fabrication. The final version has 5 sensors to be measured with a flex cable connector, plus several others for testing, and the metal leads have 45º junctions instead of right angles, to minimize damage between handling and bending. Sensors were allocated only in the peripheral region of the mask to avoid thermal cracking. To prevent open circuit between sensor and contact pads, the stripes of the first were connected with the same material, and the size of the later was increased to have greater probability of overlap between the first and second layer. This design improvement was effective, as the final fabrication batch showed little to none damageg structures.

To characterize the fabricated sensors, a setup was developed and adapted to the existing magneto-transport characterization apparatus. Instead of the common electric micro-probes, samples are inserted in a flex cable connector soldered onto a PCB that allows the electric connection between sample and acquisition system. To apply bending to the samples, supports were fabricated with different curvature radii.

AMR curves were obtained for each material deposited on different substrates and bending conditions. The tested curvature radii were r_{bend} = 12, 10 and 2.5 mm. The highest AMR ratio obtained was

0.90% in $Ni_{80}Fe_{20}$ // PI-125 µm sample, which is very close to values obtained on silicon counterparts.

In general, both AMR signal and H_{sat} values seemed to be stable even with increased curvature, which is indicative of a good resilience of both sensors and metal leads. Only on PI-25 µm a reduction in signal is observable with r_{bend} = 2.5 mm. $Co_{90}Fe_{10}$ curves yielded lower AMR ratios in general, the larger being 0.58% on PI-125 µm. Furthermore, the sample on PI-25 µm showed a strong presence of noise affecting the curves shape. This material exhibits a larger degradation in performance with increasing bending, as sample on PI-125 µm did not even reach saturation with the maximum magnetic field.

The demagnetizing field is not the dominant contribution for the overall magnetic anisotropy in the measured sensors, but if we want to achieve smaller structures with only a few micrometers wide, special attention will be required to minimize this term. Induced stress through bending depicts a strong variation with substrate thickness, as for $Ni_{80}Fe_{20}$ // PI-25 µm, $\sigma_{2.5mm}$ = 216 MPa and for PEN-75 µm, $\sigma_{2.5mm}$ = 1490 MPa. This stress can be translated to an anisotropy constant, taking into account the magnetostriction coefficient of the material. It is recognizable that for $Ni_{80}Fe_{20}$ samples the stress anisotropy plays a role on the saturation field, since both H_{sat} and H_{σ} are in the same order of magnitude, however, H_k gives almost the same contribution. On the other hand, $Co_{90}Fe_{10}$ saturation field clearly has other strong contribution besides induced stress, which probably comes from the magnetocrystalline term, as it is perceptible through the H_k value that comes from the hysteresis curve. The magnetostriction constant enhances the effect of stress, such that the magnetoelastic constant is ruled by these two parameters, the larger the magnetostriction coefficient and induced stress, the more pronounced this effect will be.

In conclusion, although PI-125 µm seems to be a better substrate for the sensor layer, as it yielded better AMR signal, it has the drawback of not reaching the same curvature as easily as PEN-75 µm and PI-25 µm. The thinner polyimide showed the lowest AMR ratio, but on the other hand it also presented the lowest saturation field and stress values, with the advantage of conforming to almost any shape. For future work, further optimization of the fabrication techniques should be performed, namely on lithography steps to improve the sensor quality and minimize alignment errors. Successful fabrication of smaller sensors of, for example, 20 µm wide should be attained in order to characterize those structures and understand if it such sizes are a viable option. Furthermore, fabrication on PEN should be further explored with smaller foil thickness to improve conformability and reduce stress on the film. PI-25 µm seems to be a very promising material for flexible applications for the reasons stated earlier, so other bending radii should be used to study in depth the potential of this polymer.

References

[1] B. Dieny, V. S. Speriosu, S. S. P. Parkin, B. A. Gurney, D. R. Wilhoit, and D. Mauri. Giant magnetoresistive in soft ferromagnetic multilayers. *Physical Review B*, 43(1):1297–1300, jan 1991. doi: 10.1103/physrevb.43.1297.

[2] F. P. P. F. R. C. S. C. F. Magnetoresistive Sensors. *Journal of Physics: Condensed Matter*, 2007.

[3] C. Zheng, K. Zhu, S. C. de Freitas, J.-Y. Chang, J. E. Davies, P. Eames, P. P. Freitas, O. Kazakova, C. Kim, C.-W. Leung, S.-H. Liou, A. Ognev, S. N. Piramanayagam, P. Ripka, A. Samardak, K.-H. Shin, S.-Y. Tong, M.-J. Tung, S. X. Wang, S. Xue, X. Yin, and P. W. T. Pong. Magnetoresistive Sensor Development Roadmap (Non-Recording Applications). *IEEE Transactions on Magnetics*, 55(4):1–30, apr 2019. doi: 10.1109/tmag.2019.2896036.

[4] M. Melzer, M. Kaltenbrunner, D. Makarov, D. Karnaushenko, D. Karnaushenko, T. Sekitani, T. Someya, and O. G. Schmidt. Imperceptible magnetoelectronics. *Nature Communications*, 6 (1), jan 2015. doi: 10.1038/ncomms7080.

[5] Z. Wang, X. Wang, M. Li, Y. Gao, Z. Hu, T. Nan, X. Liang, H. Chen, J. Yang, S. Cash, and N.-X. Sun. Highly Sensitive Flexible Magnetic Sensor Based on Anisotropic Magnetoresistance Effect. *Advanced Materials*, 28(42):9370–9377, sep 2016. doi: 10.1002/adma.201602910.

[6] P. Ripka. Magnetic Sensors: Principles and Applications. *Elsevier*, 2007.

[7] M. J. e. a. Caruso. A New Perspective on Magnetic Field Sensing. ., 1999.

[8] T.-R. Ger, H.-T. Huang, C.-Y. Huang, and M.-F. Lai. Single cell detection using 3D magnetic rolled-up structures. *Lab on a Chip*, 13(21):4225, 2013. doi: 10.1039/c3lc50721a.

[9] M. H. Kang, B. W. Choi, K. C. Koh, J. H. Lee, and G. T. Park. Experimental study of a vehicle detector with an AMR sensor. *Sensors and Actuators A: Physical*, 118(2):278–284, feb 2005. doi: 10.1016/j.sna.2004.09.002.

[10] L. Jogschies, D. Klaas, R. Kruppe, J. Rittinger, P. Taptimthong, A. Wienecke, L. Rissing, and M. Wurz. Recent Developments of Magnetoresistive Sensors for Industrial Applications. *Sensors*, 15(11):28665–28689, nov 2015. doi: 10.3390/s151128665.

[11] J.-H. Kwon, W.-Y. Kwak, and B. K. Cho. Magnetization Manipulation of a Flexible Magnetic Sensor by Controlled Stress Application. *Scientific Reports*, 8(1), oct 2018. doi: 10.1038/s41598-018-34036-z.

[12] S. MURAKAMI, E. L. BEDIA, and S. KOHJIYA. Polymer Materials. Structural Development of PEN/PET Blend Film during Drawing at High Temperature. *Journal of the Society of Materials Science, Japan*, 49(12):1263–1269, 2000. doi: 10.2472/jsms.49.1263.

[13] D. Odaka, M. Komatsu, and Y. Ohki. Observation of crystal growth in polyethylene naphthalate by terahertz spectroscopy. In *2016 IEEE International Conference on Dielectrics (ICD)*. IEEE, jul 2016. doi: 10.1109/icd.2016.7547674.

[14] J. Xu, Y. Dong, Z. Zhang, S. Li, S. He, and H. Li. Full scale strain monitoring of a suspension bridge using high performance distributed fiber optic sensors. *Measurement Science and Technology*, 27 (12):124017, nov 2016. doi: 10.1088/0957-0233/27/12/124017.

[15] D. Zymelka, K. Togashi, R. Ohigashi, T. Yamashita, S. Takamatsu, T. Itoh, and T. Kobayashi. Printed strain sensor array for application to structural health monitoring. *Smart Materials and Structures*, 26(10):105040, sep 2017. doi: 10.1088/1361-665x/aa8831.

[16] M. Melzer, D. Karnaushenko, G. Lin, S. Baunack, D. Makarov, and O. G. Schmidt. Direct Transfer of Magnetic Sensor Devices to Elastomeric Supports for Stretchable Electronics. *Advanced Materials*, 27(8):1333–1338, jan 2015. doi: 10.1002/adma.201403998.

[17] J. M. D. Coey. *Magnetism and Magnetic Materials*. Cambridge University Press, 2009. doi: 10.1017/cbo9780511845000.

[18] D. Makarov, M. Melzer, D. Karnaushenko, and O. G. Schmidt. Shapeable magnetoelectronics. *Applied Physics Reviews*, 3(1):011101, mar 2016. doi: 10.1063/1.4938497.

[19] R. J. dos Santos Macedo. *Spintronic Nano Devices: Nanofabrication of sub-50nm Magnetic Tunnel Junctions and Self-Powered Hybrid Sensors*. PhD thesis, Instituto Superior Técnico, 2011.

[20] R. Slatter. Magnetoresistive (MR) Sensors for Angle-, Path- and Current Measurement in Harsh Environments. ., 2015. doi: 10.5162/SENSOR2015/B3.1.

[21] A. N. V. da Silva. *Towards sub-100nm Magnetoresistive Devices: From Simulations to Applications*. PhD thesis, Instituto Superior Técnico, 2016.

[22] T. McGuire and R. Potter. Anisotropic magnetoresistance in ferromagnetic 3d alloys. *IEEE Transactions on Magnetics*, 11(4):1018–1038, jul 1975. doi: 10.1109/tmag.1975.1058782.

[23] V. Gehanno, P. Freitas, A. Veloso, J. Ferrira, B. Almeida, J. Soasa, A. Kling, J. Soares, and M. da Silva. Ion beam deposition of Mn-Ir spin valves. *IEEE Transactions on Magnetics*, 35(5): 4361–4367, 1999. doi: 10.1109/20.799086.

[24] J. Lenz and S. Edelstein. Magnetic sensors and their applications. *IEEE Sensors Journal*, 6(3): 631–649, jun 2006. doi: 10.1109/jsen.2006.874493.

[25] S. I. P. C. de Freitas. *Dual-Stripe GMR and Tunnel Junction Read Heads and Ion Beam Deposition and Oxidation of Tunnel Junctions*. PhD thesis, Instituto Superior Técnico, 2001.

[26] *DUPONT PEN - Datasheet*.

[27] K. A. Sierros. *Mechanical Properties and characterization of substrates for flexible displays*. PhD thesis, School of Metallurgy and Materials, The University of Birmingham, 2006.

[28] *Goodfellow PET datasheet*.

[29] *DUPONT KAPTON HN - Datasheet*.

[30] S. Yasufuku. Application of poly(ethylene naphthalate) films to electrical and audio-visual uses in Japan. *IEEE Electrical Insulation Magazine*, 12(6):8–14, nov 1996. doi: 10.1109/57.546275.

[31] A. Guittoum, A. Bourzami, A. Layadi, and G. Schmerber. Structural, electrical and magnetic properties of evaporated permalloy thin films: effect of substrate and thickness. *The European Physical Journal Applied Physics*, 58(2):20301, may 2012. doi: 10.1051/epjap/2012110343.

[32] R. Bonin, M. L. Schneider, T. J. Silva, and J. P. Nibarger. Dependence of magnetization dynamics on magnetostriction in NiFe alloys. *Journal of Applied Physics*, 98(12):123904, dec 2005. doi: 10.1063/1.2143121.

[33] P. Ripka. Magnetic sensors: Principles and applications. In *Encyclopedia of Materials: Science and Technology*, pages 1–11. Elsevier, 2007. doi: 10.1016/b978-008043152-9.02158-8.

[34] S. D. S. Cakmaktepe. Magnetic and structural analysis of sputtered Co90Fe10/Au multilayer films for magnetic recording applications. *JOURNAL OF OPTOELECTRONICS AND ADVANCED MATERIALS*, 2016.

[35] A. sciences. Magnetron sputtering. `https://www.angstromsciences.com/magnetron-sputtering-deposition`. [Online; accessed 14/05/2019].

[36] SEMICORE. Magnetron sputtering. `http://www.semicore.com/what-is-sputtering`. [Online; accessed 14/05/2019].

[37] J. D. Jarratt, T. J. Klemmer, and J. A. Barnard. Electrical resistivity in sputtered Co90Fe10/Ag GMR multilayers. *Journal of Applied Physics*, 81(8):5793–5795, apr 1997. doi: 10.1063/1.364670.

[38] J. Epp. X-ray diffraction (XRD) techniques for materials characterization. In *Materials Characterization Using Nondestructive Evaluation (NDE) Methods*, pages 81–124. Elsevier, 2016. doi: 10.1016/b978-0-08-100040-3.00004-3.

[39] B. D. CULLITY. *Elements of x-rays diffraction*. Addison-Wesley Publishing Company, Inc, 1956.

[40] J. Megusar. Low temperature fast-neutron and gamma irradiation of Kapton® polyimide films. *Journal of Nuclear Materials*, 245(2-3):185–190, jun 1997. doi: 10.1016/s0022-3115(97)00012-3.

[41] Y.-T. Chen, S. H. Lin, and Y. C. Lin. Effect of Low-Frequency Alternative-Current Magnetic Susceptibility inNi80Fe20Thin Films. *Journal of Nanomaterials*, 2012:1–6, 2012. doi: 10.1155/2012/186138.

[42] S. Sheng, W. Li, M. Li, and G. Yu. Investigation on interface of NiFeCr/NiFe/Ta films with high magnetic field sensitivity. *Rare Metals*, 31(1):22–26, jan 2012. doi: 10.1007/s12598-012-0455-1.

[43] S. Cakmaktepeand and S. Diken. Magnetic and structural analysis of sputtered Co90Fe10/Au multilayer films for magnetic recording applications. *Journal of Optoelectronics and Advanced Materials, 18, p107-111*, 2016.

[44] Y. K. Kim. Soft magnetic properties of sub 10 nm NiFe and Co films encapsulated with Ta or Cu. *physica status solidi (a)*, 201(8):1859–1861, jun 2004. doi: 10.1002/pssa.200304601.

[45] S. Merabtine, F. Zighem, A. Garcia-Sanchez, V. Gunasekaran, M. Belmeguenai, X. Zhou, P. Lupo, A. O. Adeyeye, and D. Faurie. Origin of relationship between ferromagnetic response and damage in stretched systems. *Scientific Reports*, 8(1), sep 2018. doi: 10.1038/s41598-018-32149-z.

[46] J. Rittinger, P. Taptimthong, L. Jogschies, M. C. Wurz, and L. Rissing. Impact of different polyimide-based substrates on the soft magnetic properties of NiFe thin films. In J. L. Sánchez-Rojas and R. Brama, editors, *Smart Sensors, Actuators, and MEMS VII and Cyber Physical Systems*. SPIE, may 2015. doi: 10.1117/12.2178765.

[47] A. Koh, W. Hu, R. Wilson, S. Wang, and R. Sinclair. Preparation, structural and magnetic characterization of synthetic anti-ferromagnetic (SAF) nanoparticles. *Philosophical Magazine*, 88(36): 4225–4241, dec 2008. doi: 10.1080/14786430802585133.

[48] A. International. Chapter 2: Thermal expansion. Technical report, The Materials Information Society, 2002.

[49] T. NAGAYAMA, Y. MIZUTANI, T. NAKAMURA, and N. SHINOHARA. Thermal Expansion Properties of Nickel-Iron Alloy Electrodeposits. *Journal of The Surface Finishing Society of Japan*, 57(10):733–737, 2006. doi: 10.4139/sfj.57.733.

[50] Y. Y. Hu and W. M. Huang. Thermal Stress Analysis and Characterization of Thermomechanical Properties of Thin Films on an Elastic Substrate. In *Handbook of Manufacturing Engineering and Technology*, pages 1–71. Springer London, 2013. doi: 10.1007/978-1-4471-4976-7_51-1.

[51] X. Tang, W. Du, J. Yu, H. Zhang, and H. Su. A flexible way to modulate the detection range of anisotropic magnetoresistance by exchange bias field. *Journal of Magnetism and Magnetic Materials*, 476:469–471, apr 2019. doi: 10.1016/j.jmmm.2019.01.012.

[52] T. Griesbach, M. C. Wurz, and L. Rissing. Design, Fabrication, and Testing of a Modular Magnetic Field Microsensor on a Flexible Polymer Foil. *IEEE Transactions on Magnetics*, 48(11):3843–3846, nov 2012. doi: 10.1109/tmag.2012.2198798.

[53] S. Srichandan. *Electrical and thermal transport coefficients of CoFe thin films deposited on a microcalorimeter*. PhD thesis, Universitat Regensburg, 2016.

[54] M. Gueye, P. Lupo, F. Zighem, D. Faurie, M. Belmeguenai, and A. O. Adeyeye. Unambiguous magnetoelastic effect on residual anisotropy in thin films deposited on flexible substrates. *EPL (Europhysics Letters)*, 114(1):17003, apr 2016. doi: 10.1209/0295-5075/114/17003.

[55] S. Jo and M. Seigler. Magnetostriction and stress of Ta/(Cu/Co90Fe10)xN/Ta multilayer films. *Applied Physics Letters*, 80(1):82–84, jan 2002. doi: 10.1063/1.1409271.

[56] C.-Y. Hung, M. Mao, S. Funada, T. Schneider, L. Miloslavsky, M. Miller, C. Qian, and H. C. Tong. Magnetic properties of ultrathin NiFe and CoFe films. *Journal of Applied Physics*, 87(9):6618–6620, may 2000. doi: 10.1063/1.372789.

Appendix A

Runsheets

A.1 Fabrication process runsheet

Run Sheet – AMR samples

Responsible: Catarina Janeiro

STEP 1: Substrate preparation

Machine: Workbench and ultrasounds

Substrate: PEN film (75 µm) / Polyimide Film (25 and 125 µm)

Conditions:

- Alconox and Ultrasounds (no temperature) for both substrates;
- Typically 30 min are enough, but if it's seen at naked eye that the substrate is not clean, do another 30 min;
- PEN and 125 PI can be cleaned vertically in the coplin jar, but 25 PI will adhere to the wall of the container, so it has to be cleaned horizontally in a glass beaker;

STEP 2: Film deposition

Substrate	Ta 100 / CoFe 200 / Ta 100	Ta 100 / NiFe 200 / Ta 100	Ta 100 / Ni 200 / Ta 100
PI (25 µm)			
PI (125 µm)			
PEN (75 µm)			

Deposition conditions (write read values, batch/wafer recipe, process steps, B.P.):

- **Ni in Alcatel:** 30 W (RF) / 20 sccm / Deposition rate ~ 0,11 A/s / 200 Å / 1.86 mTorr
- **CoFe (N2000):** 49 W (RF) / 209 V / 9.7 sccm / 8.2 mTorr / 200 A
- **Ta (N2000):** 10 W (DC) / 390 V / 30 mA / 10.3 sccm / 4.7 mTorr

STEP 3: 1st Lithography (sensors definition)

1) Photoresist spin coating

Machine: Automatic Coating Track System

O Coat 1.5 µm PR (Recipe 6/2)

Coating Parameters	
First Step	Dispense photoresist on the sample and spinning at 800 rpm for 5 sec.
Second step	Spin at 2500 rpm for 30 sec. to obtain ~1.45µm thickness.
Third step	Soft bake at 85ºC for 60 seconds.

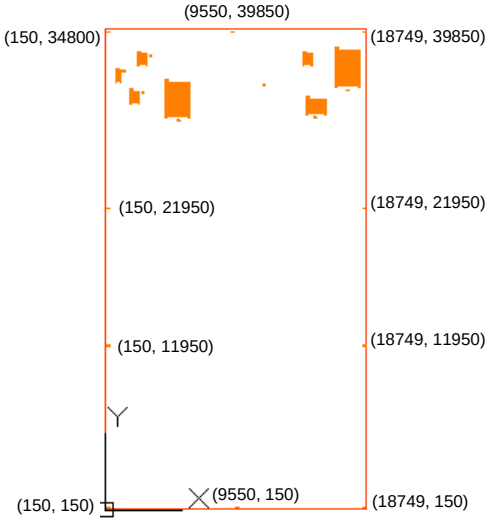

2) Lithography

Machine: DWL

Mask	**CJ_AMR_V4_L1**	**Layer**	Sensor (L1) (INVERTED)
Die size	19000 x 35000	Nr of Dies	1
		Map	AMSION_C
(0,0) position	3000, 3000	Alignment marks (from (0,0))	-
Power	100mW w/ grey filter	Energy	85.m12
		Focus	10

3) Develop: Recipe 6/manual

Developer: TMA238WA

Development parameters:
Bake at 85°C for 60s
Cool for 30s
Developer for 60s

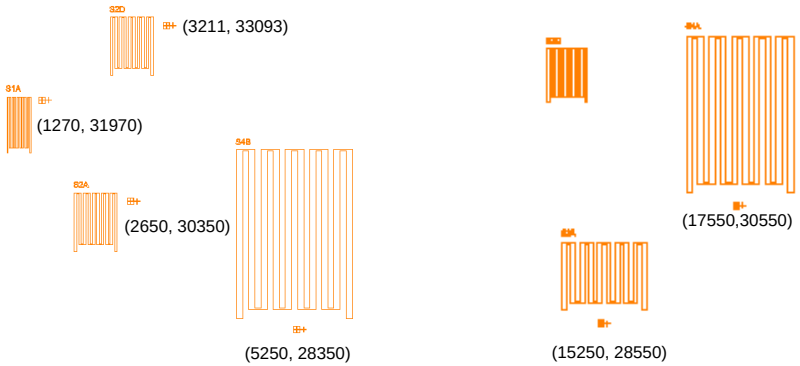

Layer one sensors close up and alignment coordinates.

STEP 4: 1st Etch (Ion Milling)

Machine: N3000			B.P = 3 x 10^{-7} Torr
Sample ID	Total to etch (Å)	Etch rate	t(s)
	400	~1 Å/s @60ºpan (NiFe) ~0,5 Å/s @60ºpan (CoFe)	

Batch Recipe:

Slot#	Wafer Recipe	Process Steps

Set-Points: 54 W / +500 V / -200 V / 8 sccm

Read conditions

	RF Power (W)	V_+(V)	I_+(mA)	V_-(V)	I_-(mA)	Gas flux (sccm)	W.P (torr)
Assist Gun							

***Notes*:**

- Sample should be stretched and flatten to its best in the etching wafer to guarantee a uniform etch;
- The back of the sample to be etched and the etching wafer used should be cleaned with acetone before etching in order to avoid unwanted PR to burn and enhance better thermal contact.

Optical Inspection

STEP 5: Photoresist Strip

Machine: Chemical Workbench + Ultrasounds

Conditions: Acetone bath + ultrasounds (no temperature)

Start: **Total time:**

***Notes*:**

- Ultrassonic time can be from 5-10 min, depending on the substrate and how long has been since exposure;
- In acetone, PI 25 will roll itself in a tube, so in order to promote a good and fast strip, it should be rinsed with IPA several times;

Optical Inspection:

STEP 6: 2st Lithography (Contact leads definition)

1) Photoresist spin coating

Machine: Automatic Coating Track System

O Coat 1.5 µm PR (Recipe 6/2)

Coating Parameters	
First Step	Dispense photoresist on the sample and spinning at 800 rpm for 5 sec.
Second step	Spin at 2500 rpm for 30 sec. to obtain ~1.45µm thickness.
Third step	Soft bake at 85ºC for 60 seconds.

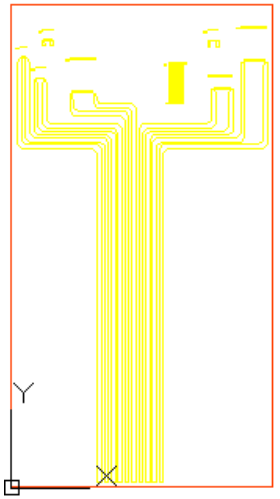

Notes: Let the wafer cool slowly at room temperature after the soft bake, as a rapid cooling is more probable to cause cracks on the film.

Use Pre-Development for 20s

Manually do a 20 seconds pre-development on **track 1 station 2**

2) Lithography

Machine: DWL

Mask	**CJ_AMR_V4_L2**	**Layer**	Contact pads **(NON-INVERTED)**
Die size	19 000 x 35 000	Nr of Dies	1
		Map	AMSION_C
(0,0) position	The best alignment mark from the previous lithography	Alignment marks (from (0,0))	The best alignment mark from the previous lithography
Power	100mW w/ grey filter	Energy	95.m12
		Focus	10

3) Develop: Recipe 6/manual Developer: TMA238WA

Development parameters:
Bake at 85°C for 120s
Cool for 30s
Developer for 60s

Don't forget optical inspection!!

STEP 7: Contact leads deposition

Machine: Alcatel

Notes:

- Deposit 2 calibration bars (Glass and polymer) for thickness and resistivity control;

	Reference Deposition Rate (Å/s)	Deposition time (s)
Cr	0.7	**2 min 30 s**
Au	0.9	**18 min**

Deposition conditions:

- Cr (DC): 100 Å / 20 W / 20 sccm / 2.6 mTorr
- Au (RF): 1000 Å / 30 W / 20 sccm / 2.6 mTorr

STEP 8: Lift-Off

Machine: Wet Bench + Ultrasounds

Conditions: Acetone bath + ultrasounds (no temperature)

Start: **Total time:**

***Notes*:**

- Ultrassonic time can be from 5-10 min, depending on the substrate and how long has been since exposure;
- In acetone, PI 25 will roll itself in a tube, so in order to promote a good and fast strip, it should be rinsed with IPA several times;

Optical Inspection: